The Astrophysical Journal, 888:72 (16pp), 2020 January 10 https://doi.org/10.3847/1538-4357/ab5d2b

The Detection of Dust Gap-ring Structure in the Outer Region of the CR Cha Protoplanetary Disk

Seongjoong Kim[1], Sanemichi Takahashi[2,3], Hideko Nomura[1,2], Takashi Tsukagoshi[2], Seokho Lee[2], Takayuki Muto[4], Ruobing Dong[5], Yasuhiro Hasegawa[6], Jun Hashimoto[7], Kazuhiro Kanagawa[8], Akimasa Kataoka[2], Mihoko Konishi[9], Hauyu Baobab Liu[10], Munetake Momose[11], Michael Sitko[12,13], and Kengo Tomida[14]
[1] Department of Earth and Planetary Sciences, Tokyo Institute of Technology, 2-12-1 Ookayama, Meguro-ku, Tokyo 152-8551, Japan
[2] National Astronomical Observatory of Japan, 2-21-1 Osawa, Mitaka, Tokyo 181-8588, Japan
[3] Department of Applied Physics, Kogakuin University, 1-24-2 Nishi-Shinjuku, Shinjuku-ku, Tokyo, 163-8677, Japan
[4] Division of Liberal Arts, Kogakuin University, 1-24-2 Nishi-Shinjuku, Shinjuku-ku, Tokyo 163-8677, Japan
[5] Department of Physics & Astronomy, University of Victoria, Victoria, BC V8P 1A1, Canada
[6] Jet Propulsion Laboratory, California Institute of Technology, Pasadena, CA 91109, USA
[7] Astrobiology Center, National Institutes of Natural Sciences, 2-21-1 Osawa, Mitaka, Tokyo 181-8588, Japan
[8] Research Center for the Early Universe, Graduate School of Science, University of Tokyo, Hongo, Bunkyo-ku, Tokyo 113-0033, Japan
[9] Faculty of Science and Technology, Oita University, 700 Dannoharu, Oita 870-1192, Japan
[10] Academia Sinica Institute of Astronomy and Astrophysics, P.O. Box 23-141, Taipei 10617, Taiwan
[11] College of Science, Ibaraki University, 2-1-1 Bunkyo, Mito, Ibaraki 310-8512, Japan
[12] Department of Physics, University of Cincinnati, Cincinnati, OH 45221, USA
[13] Space Science Institute, 475 Walnut Street, Suite 205, Boulder, CO 80301, USA
[14] Department of Earth and Space Science, Osaka University, Toyonaka, Osaka 560-0043, Japan
Received 2019 September 21; revised 2019 November 16; accepted 2019 November 27; published 2020 January 9

Abstract

We observe the dust continuum at 225 GHz and CO isotopologue (^{12}CO, ^{13}CO, and C^{18}O) $J = 2$–1 emission lines toward the CR Cha protoplanetary disk using the Atacama Large Millimeter/submillimeter Array. The dust continuum image shows a dust gap-ring structure in the outer region of the dust disk. A faint dust ring is also detected around 120 au beyond the dust gap. The CO isotopologue lines indicate that the gas disk is more extended than the dust disk. The peak brightness temperature of the ^{13}CO line shows a small bump around 130 au, while ^{12}CO lines do not. We investigate two possible mechanisms for reproducing the observed dust gap-ring structure and a gas temperature bump. First, the observed gap structure can be opened by a Jupiter-mass planet using the relation between the planet mass and the gap depth and width. Meanwhile, the radiative transfer calculations based on the observed dust surface density profile show that the observed dust ring could be formed by dust accumulation at the gas temperature bump, that is, the gas pressure bump produced beyond the outer edge of the dust disk.

Unified Astronomy Thesaurus concepts: Observational astronomy (1145); Proplyds (1296)

1. Introduction

CR Cha (aka Sz 6, Cha T8) is a K-type pre-main-sequence star (Hussain et al. 2009; Villebrun et al. 2019) in the Cha I dark cloud, one of the famous star-forming clouds in our Galaxy. The fitting on the stellar evolution tracks suggests that the stellar mass of CR Cha is $M_\star = 1.2$–$2\,M_\odot$, with an age of 1–3 Myr (e.g., D'Antona & Mazzitelli 1994; Natta et al. 2000; Hussain et al. 2009; Varga et al. 2018). The latest updated distance of CR Cha is $d \sim 187.5 \pm 0.8$ pc (*Gaia* DR2; Gaia Collaboration et al. 2018). The existence of the protoplanetary disk around CR Cha had already been revealed by the thermal dust emission at (sub) millimeter wavelengths (e.g., Ubach et al. 2012; Pascucci et al. 2016; Ribas et al. 2017; Ubach et al. 2017).

The spectral index α at millimeter wavelength is linked to the dust properties, such as dust opacity and the dust grain size (e.g., Miyake & Nakagawa 1993). It can be used to study the dust growth in the disk by comparing with the spectral index of the interstellar medium (ISM; e.g., Beckwith & Sargent 1991; D'Alessio et al. 2001). Toward the CR Cha disk, the measured spectral index at 1 mm is $\alpha_{1\ \mathrm{mm}} \sim 3.4$ (Ubach et al. 2012), which is close to $\alpha_{\mathrm{ISM}} \sim 3.7$ in the ISM. This large $\alpha_{1\ \mathrm{mm}}$ value in the CR Cha disk indicates that the maximum grain size is small in the outer disk (e.g., Draine 2006). This may be the result of the dust growth in this region: the millimeter-sized dust grains already drifted inward in the gas disk owing to the gas drag (Ribas et al. 2017; Ubach et al. 2017). Recent CO line surveys toward the protoplanetary disks in the Cha I cloud using Atacama Large Millimeter/submillimeter Array (ALMA) can support this possibility by detecting that the gas disk around CR Cha exists with an angular size of $\sim 0\farcs9$ in radius (Long et al. 2017).

However, the timescale of the radial drift of millimeter/centimeter-sized dust grains (10^{4-5} yr; e.g., Takeuchi & Lin 2005; Brauer et al. 2007) is much shorter than the age of CR Cha ($\sim$1–3 Myr). Ribas et al. (2017) suggested that some braking mechanisms, such as dust trapping at the pressure bumps produced by zonal flow (e.g., Pinilla et al. 2012) or planet-opened gaps (e.g., Zhu et al. 2012), are required to stop or slow down the radial drift of the dust grains. That is, the CR Cha disk is one of the strong candidates that would have disk substructures like a dust ring/gap.

In this paper, we show the results of the dust continuum and the CO isotopologue $J = 2$–1 emission lines observed at ALMA Band 6 to examine the existence of small-scale disk substructure like a gap or ring structure in the CR Cha disk. We summarize the information of ALMA observations toward the CR Cha disk in Section 2. The observed dust continuum and CO isotopologue images are presented in Section 3. In Section 4, we discuss the radial profiles of dust surface density and CO gas column density derived from the observations and the possible mechanisms to explain the detected CR Cha disk structure. Finally, we summarize our results in Section 5.

Table 1
Summary of Dust Continuum and CO Isotopologue Line Images

Species	$\nu_{\rm center}$ (GHz)	rms in Cube (mJy beam^{-1})	rms in Mom. 0 (mJy beam^{-1} km s^{-1})	Beam Size (arcsec^2)	Beam PA (deg)
Dust	225	∼0.0178	⋯	0.087 × 0.052	35.75
^{12}CO	230.538	∼2.47	∼4.594	0.188 × 0.128	0.635
^{13}CO	220.398	∼2.40	∼4.978	0.196 × 0.143	0.405
C^{18}O	219.560	∼2.28	∼3.441	0.194 × 0.142	0.976

2. Observation

The CR Cha protoplanetary disk was observed at ALMA Band 6 on 2017 November and 2018 March with 47 and 42 antennae, respectively (2017.1.00286.S). The projected baselines are from 12.54 m to 7.908 km, corresponding to a maximum angular coverage of ∼5″ and an angular resolution of $\gtrsim$0.″06. The total execution time for the observations is ∼3.2 hr, including the target on-source time of ∼2 hr. J1427–4206 and J0635–7516 are used for the bandpass and flux calibrations at each observation. J1058–8003 is selected as a phase calibrator at both observations.

The correlator setup has four spectral windows (SPWs). Dust continuum emission is observed at 233 GHz (SPW1) and 217 GHz (SPW2) with 1.8 GHz bandwidth at each SPW. For the CO isotopologue emission lines, the SPWs are centered at 230.538 GHz for ^{12}CO (SPW0), 220.398 GHz for ^{13}CO, and 219.560 GHz for C^{18}O (SPW3). The spectral resolution for three CO isotopologue lines is 61 kHz, corresponding to ∼0.08 km s^{-1} in velocity.

The basic calibration steps are progressed through the ALMA calibration pipeline using `CASA` package version 5.3. After the ALMA pipeline calibration, we make the images of dust continuum and CO isotopologue emission lines by the `CLEAN` command in `CASA`. The Briggs robust = 0 is used for the dust continuum image, obtaining the synthesized beam size of ∼0.″087 × 0.″052 and the beam position angle (PA) of ∼35.°75. The phase self-calibration is applied to the dust continuum image for improving the data quality. Meanwhile, the Briggs robust = 2.0 (natural weighting) is applied for the CO isotopologue lines to obtain high signal-to-noise ratios (S/Ns) of ∼20–30. We also apply the phase self-calibration to the CO line data, but the images are not improved. We note that the S/Ns of the CO isotopologue lines are ∼5–7 with ∼0.″080 × 0.″047 synthesized beam size when the robust = 0 is applied. The synthesized beam size is ∼0.″188 × 0.″128 for the ^{12}CO line, ∼0.″196 × 0.″143 for the ^{13}CO line, and ∼0.″194 × 0.″142 for C^{18}O line. Table 1 summarizes the angular resolution and rms noise level of the observed data.

3. Result

3.1. The Images of Dust Continuum and CO Isotopologue Emission Lines

Figure 1(a) shows the dust continuum image at 225 GHz. There is a dust gap at $r \sim 90$ au and a faint dust ring just beyond the dust gap. The total flux density of the dust disk is ∼0.139 Jy. It is consistent with the previous observation of $F \sim 0.125$ Jy at 1.2 mm continuum (Ubach et al. 2012). The 1σ rms level of dust continuum image is ∼0.0178 mJy beam^{-1}. The peak intensity of the dust ring is ∼10σ rms level on average. We obtain the disk geometry by the ellipse fitting using the `imfit` command in the `CASA` package. The estimated inclination of the disk is 31.°0 ± 1.°4, and disk PA is 36.°2 ± 1.°8.

Figures 1(b)–(d) show the integrated intensity maps (moment 0 maps) of the continuum-subtracted line emissions of ^{12}CO, ^{13}CO, and C^{18}O, respectively. The white dashed ellipse presents the annulus at $r = 90$ au, which corresponds to the dust gap in Figure 1(a). The cyan dashed ellipse indicates the outer edge of the CO gas disk at $r = 240$ au. This radius corresponds to the detection limit of the CO isotopologue lines, where the peak intensity at each pixel (the moment 8 map; Figures 4(a) and (b)) is ∼7.5 mJy beam^{-1}, ≈3σ rms level of the data cubes of the CO isotopologue lines. They show that the gas disk of CR Cha is much more extended than the dust disk.

The solid lines in Figure 2 present the averaged spectra of (a) ^{12}CO, (b) ^{13}CO, and (c) C^{18}O line emission inside the disk radius of $r \lesssim 240$ au, applying a disk inclination of 31° and a disk PA of 36.°2. There is a strong absorption feature at the velocity of ∼4.5 km s^{-1} in the ^{12}CO and ^{13}CO spectra. The absorption feature in C^{18}O line spectrum is less prominent than those of ^{12}CO and ^{13}CO. This absorption feature is also well seen in the channel maps (see the Appendix) and the moment 8 maps of ^{12}CO and ^{13}CO lines (see Figures 4(a) and (b)).

We perform the least mean square fitting for the emission and absorption lines to measure their strengths, velocity centers, and width. We use the following function for the fitting:

$$I_\nu = A_{\rm emit} \exp\left(-\frac{(V - V_{\rm emis})^2}{2\Delta V_{\rm emis}^2}\right) + A_{\rm abs} \exp\left(-\frac{(V - V_{\rm abs})^2}{2\Delta V_{\rm abs}^2}\right). \quad (1)$$

The fitting parameters are summarized in Table 2. The dashed lines in Figure 2 show the fitting results of the emission plus absorption profiles. The fitting results show that the CO emission lines are centered at ∼5.3 km s^{-1} with $\Delta V_{\rm emis}$ of ∼2.7 km s^{-1} on average, and the absorption feature is centered at ∼4.5 km s^{-1} with $\Delta V_{\rm abs}$ of ∼0.2–0.5 km s^{-1}. These absorption features may occur as a result of the foreground Cha I molecular clouds with a system velocity of ∼4–5 km s^{-1} (e.g., Haikala et al. 2005; Long et al. 2017).

3.2. The Azimuthally Averaged Intensity Profiles

To investigate the radial structure of dust and gas disks, we make the azimuthally averaged radial profiles of the images in Figure 1. The derived disk inclination of 31° and disk PA of 36.°2 are applied to calculate the projected disk radius of each pixel. We azimuthally average every 8 au width annulus inside $r \lesssim 240$ au. As mentioned in Section 3.1, the CO isotopologue lines are affected by the absorption feature in the northern half-disk against the disk minor axis. We azimuthally average only the southern half-disk (PA = 126.°2–306.°2, counterclockwise

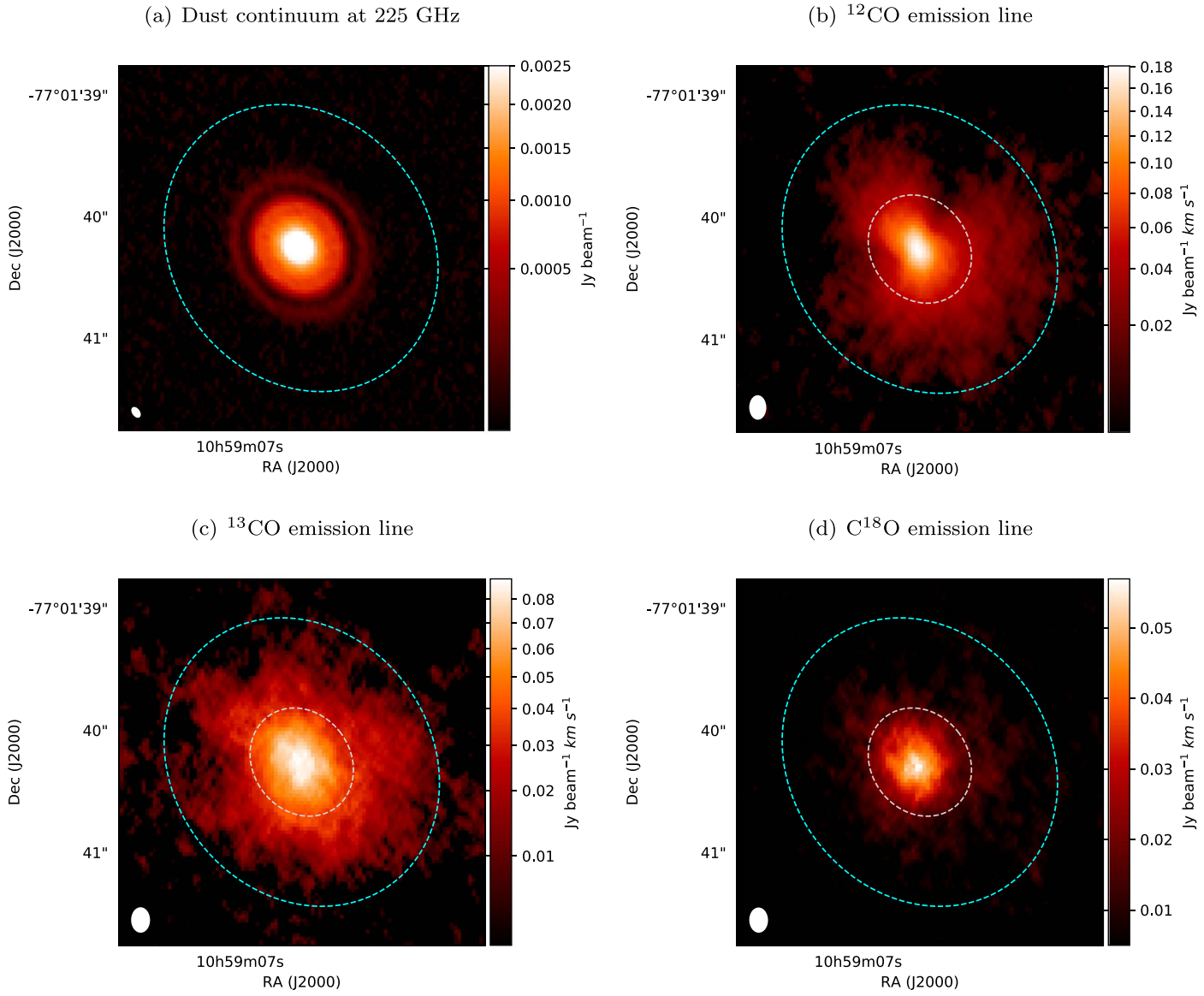

Figure 1. (a) The 225 GHz dust continuum image and the moment 0 maps of (b) ^{12}CO, (c) ^{13}CO, and (d) C^{18}O $J = 2$–1 line emission of the CR Cha disk. The synthesized beam is presented in the lower left corner: $\sim 0\farcs087 \times 0\farcs052$ for the dust continuum emission (Briggs robust = 0), $\sim 0\farcs188 \times 0\farcs128$ for ^{12}CO, $\sim 0\farcs196 \times 0\farcs143$ for ^{13}CO, and $\sim 0\farcs194 \times 0\farcs142$ for C^{18}O line emission (Briggs robust = 2). The color bar indicates the observed intensity in Jy beam^{-1} units for the dust continuum and the integrated intensities in Jy beam^{-1} km s^{-1} units for the CO isotopologue lines. The white dashed ellipse shows the location of the dust gap at $r = 90$ au. A faint dust ring is detected beyond the dust gap. The cyan dashed ellipse indicates the outer edge of the CO gas disks at $r = 240$ au.

Table 2
Summary of Gaussian Fitting Parameters for the Emission and Absorption of the CO Isotopologue Lines

Species	$A_{\rm emis}$ (mJy beam^{-1})	$V_{\rm emis}$ (km s^{-1})	$\Delta V_{\rm emis}$ (km s^{-1})	$A_{\rm abs}$ (mJy beam^{-1})	$V_{\rm abs}$ (km s^{-1})	$\Delta V_{\rm abs}$ (km s^{-1})
^{12}CO	6.37 ± 0.22	5.30 ± 0.07	2.67 ± 0.07	−10.26 ± 0.34	4.46 ± 0.02	0.52 ± 0.02
^{13}CO	5.00 ± 0.11	5.19 ± 0.06	2.64 ± 0.06	−9.97 ± 0.30	4.50 ± 0.01	0.25 ± 0.01
C^{18}O	1.90 ± 0.08	5.51 ± 0.13	2.96 ± 0.13	−1.24 ± 0.26	4.56 ± 0.05	0.21 ± 0.05

from the north) for the CO isotopologue lines to avoid the absorption feature. Meanwhile, since the dust continuum is not affected by the line absorption, we average the full azimuthal angles for the dust continuum image.

Figure 3(a) presents the azimuthally averaged radial profile of dust continuum (black) in Jy arcsec^{-2} units. The figure also shows the azimuthally averaged integrated intensity radial profiles of ^{12}CO (red), ^{13}CO (green), and C^{18}O (blue) line in Jy arcsec^{-2} km s^{-1} units. We integrate the intensities of the CO isotopologue lines within the same velocity range from ~ -1 to 12 km s^{-1}. The color-shaded regions indicate the uncertainties of the (integrated) intensity profiles due to the azimuthal average. As shown in Figure 1(a), there is a dust gap at $r \sim 90$ au and a dust ring at $r \sim 120$ au. Compared with the

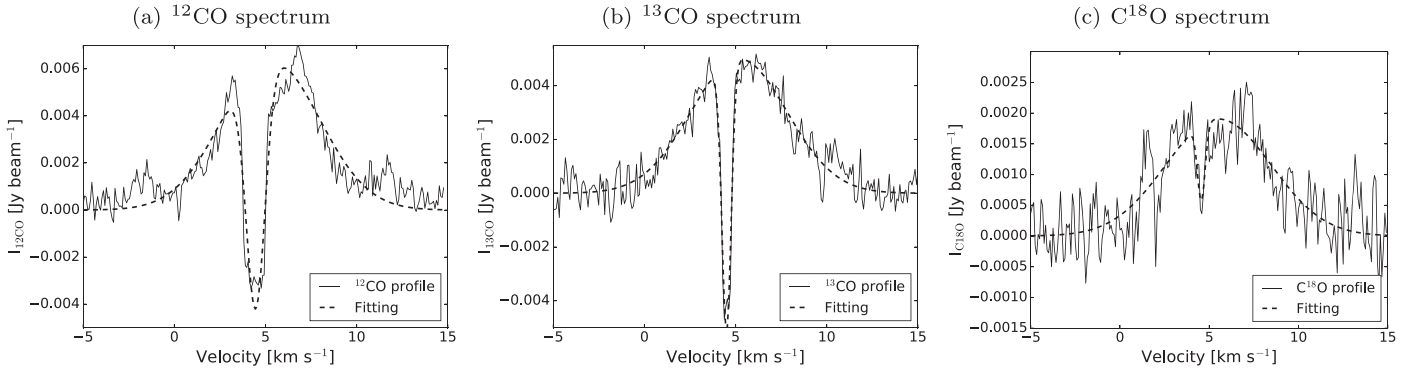

Figure 2. Averaged spectra (solid line) of (a) ^{12}CO, (b) ^{13}CO, and (c) C^{18}O $J = 2$–1 emission lines inside the disk radius of $r \lesssim 240$ au. The dashed lines are the Gaussian fitting of the emission plus absorption profiles. The emission lines are centered at ∼5.3 km s^{-1} with $\Delta V_{\rm emis}$ of ∼2.7 km s^{-1} on average. The absorption features are centered at ∼4.5 km s^{-1} with $\Delta V_{\rm abs}$ of ∼0.2–0.5 km s^{-1}. The fitting parameters are summarized in Table 2.

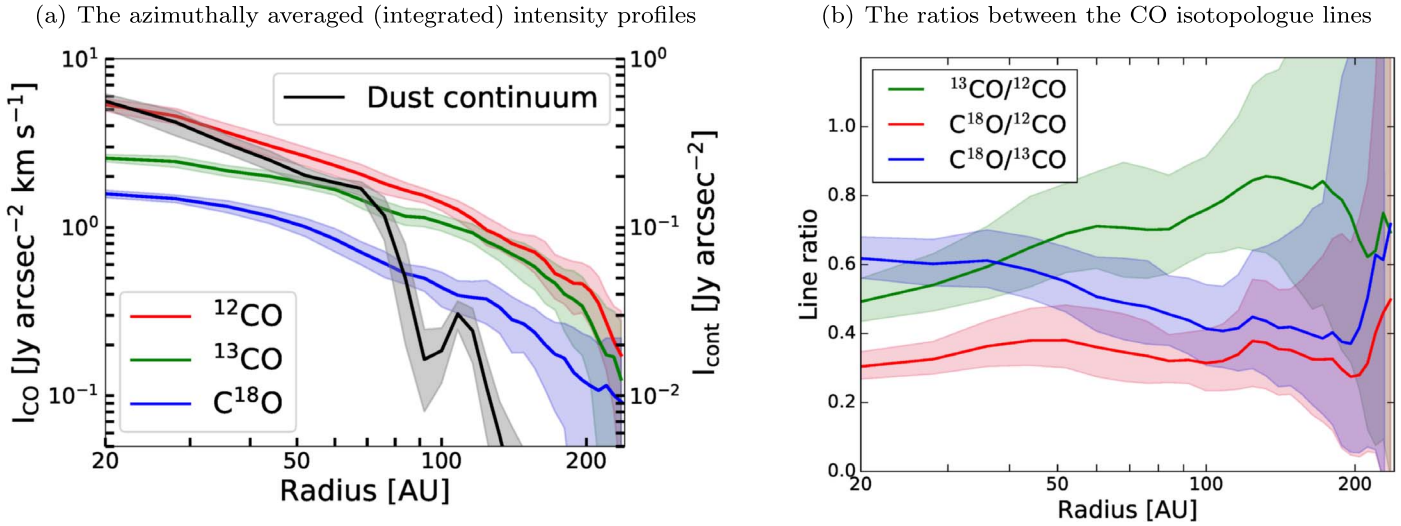

Figure 3. (a) Azimuthally averaged radial profiles of the dust continuum emission (black) in Jy arcsec^{-2} units and the integrated intensities of ^{12}CO (red), ^{13}CO (green), and C^{18}O (blue) emission lines in Jy arcsec^{-2} km s^{-1} units. The color-shaded regions indicate the uncertainty due to the azimuthal average. The dust continuum emission shows a gap at ∼90 au and a ring at ∼120 au. Meanwhile, the CO isotopologue emissions extend to $r \sim 240$ au smoothly. (b) Ratios between the azimuthally averaged integrated intensity profiles of the CO isotopologue lines: ^{13}CO/^{12}CO (green), C^{18}O/^{12}CO (red), and C^{18}O/^{13}CO (blue). The color-shaded regions show the uncertainty due to those of azimuthally averaged integrated CO intensity profiles.

rapid drop of the dust continuum intensity around 90 au, the CO isotopologue emission lines are extended to $r \sim 240$ au.

Figure 3(b) presents the ratios between the azimuthally averaged integrated intensities of the CO isotopologue lines: ^{13}CO/^{12}CO (green), C^{18}O/^{12}CO (red), and C^{18}O/^{13}CO (blue). The color-shaded regions indicate the uncertainties of the line ratios due to those of azimuthally averaged integrated CO intensities in Figure 3(a). We note that even if we derive the line ratios by dividing the moment 0 maps first and then averaging azimuthally, the results are identical inside 200 au. In the region outside of 200 au, the signals are weak so that the line ratios have very large uncertainties.

The line ratios show that the ^{12}CO and ^{13}CO lines are optically thick toward the CR Cha disk because the measured line ratios between three CO isotopologue emission lines are larger than 0.2 at all radii, which is larger than the typical abundance ratio of ^{13}CO:^{12}CO = 1:67 and C^{18}O:^{13}CO = 1:7 in protoplanetary disks (e.g., Qi et al. 2011). When the molecular lines are optically thin, the line ratios should be almost the same as the abundance ratios because the line strength is proportional to the column density of the molecules. Meanwhile, when the lines are optically thick, the intensity at the line center becomes the same as the blackbody radiation and irrelevant to the molecular abundances. Thus, the line ratios do not need to be close to the abundance ratios.

3.3. The Peak Brightness Temperatures of the CO Isotopologue Lines

Since ^{12}CO and ^{13}CO lines are optically thick, we can adapt the brightness temperature of these lines as a gas temperature. To estimate the CO gas temperature, we make the moment 8 maps of ^{12}CO and ^{13}CO emission lines using the `immoments` command in `CASA`. The moment 8 map shows the peak intensity ($I_{\nu,\rm peak}$) at each pixel in the data cube. For making the moment 8 maps, we used the data cube of ^{12}CO and ^{13}CO emission lines without dust continuum subtraction. The line plus continuum intensity should be used in order to derive the gas temperature from the peak brightness temperature of an optically thick line (e.g., Weaver et al. 2018).

Figures 4(a) and (b) present the moment 8 maps of ^{12}CO and ^{13}CO line emissions including the dust continuum. The white

(a) The moment 8 map of ^{12}CO line emission

(b) The moment 8 map of ^{13}CO line emission

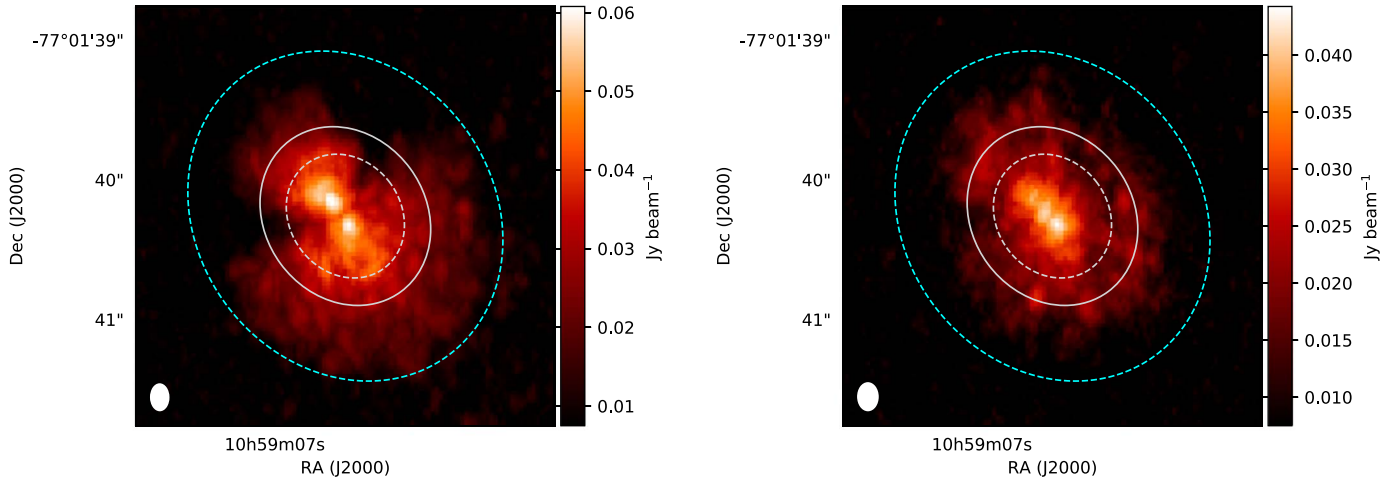

(c) The azimuthally averaged $I_{\nu,\mathrm{peak}}$ profile

(d) The $T_{\mathrm{B,peak}}$ profile

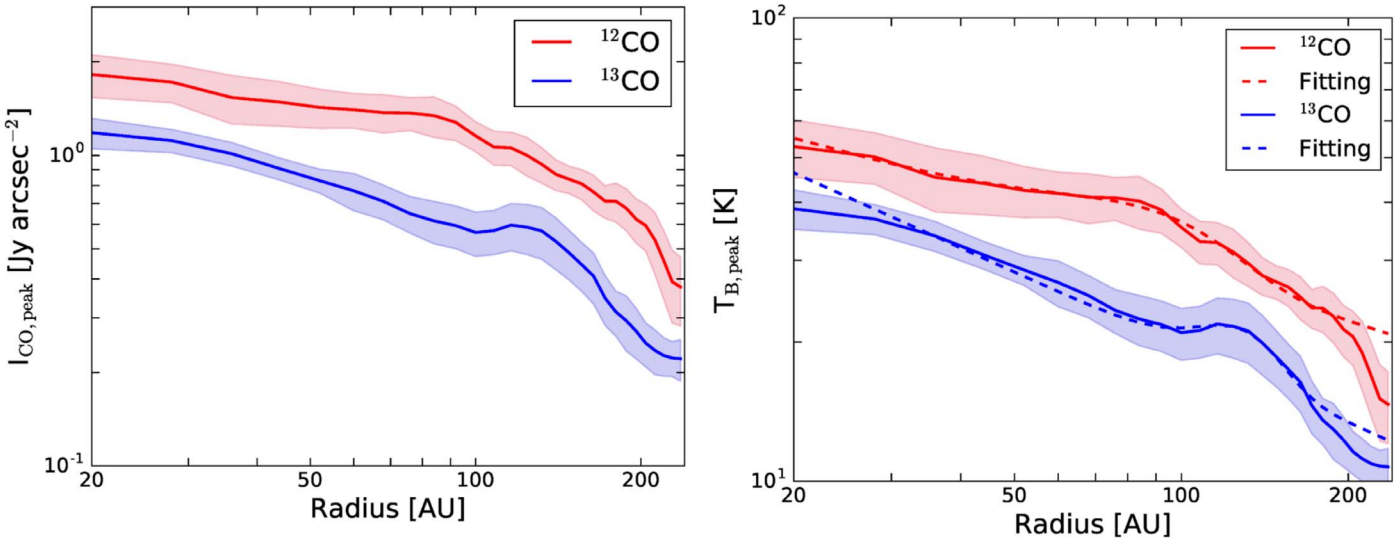

Figure 4. Moment 8 maps of (a) ^{12}CO and (b) ^{13}CO line emission with dust continuum. The absorption feature is seen in the northern half-disk. The overlaid white and cyan dashed ellipses are the same as those in Figure 1. The white solid contour indicates the location of the bump at 130 au in the azimuthally averaged ^{13}CO peak intensity radial profile. (c) Azimuthally averaged radial profiles of the peak intensity ($I_{\nu,\mathrm{peak}}$) of ^{12}CO (red) and ^{13}CO (blue) lines in the southern half-disk, which is not affected by the absorption features. The color-shaded regions indicate the uncertainties due to the azimuthal average. There is a small bump in $I_{^{13}\mathrm{CO,peak}}$ around 130 au. (d) Radial profiles of the peak brightness temperature ($T_{B,\mathrm{peak}}$) derived from the $I_{\nu,\mathrm{peak}}$ of ^{12}CO (red) and ^{13}CO (blue) lines. The color-shaded regions indicate the uncertainties propagated from those of $I_{\nu,\mathrm{peak}}$. The dashed lines present the least-squares fitting results with Equation (2). The derived $T_{B,\mathrm{peak}}$ from the $I_{^{13}\mathrm{CO,peak}}$ profile also shows a small bump at $r \sim 130$ au.

and cyan ellipses are the same as those in Figure 1. The white solid contour indicates the location of the bump at 130 au in the peak intensity and the peak brightness temperature of ^{13}CO line emission in Figures 4(c) and (d). We azimuthally average only the southern half-disk of the moment 8 maps to derive the $I_{\nu,\mathrm{peak}}$ radial profiles for avoiding the absorption feature. Figure 4(c) shows the derived $I_{\nu,\mathrm{peak}}$ radial profiles of ^{12}CO (red) and ^{13}CO (blue) lines. The color-shaded regions present the uncertainties due to the azimuthal average. The I^{13}CO, peak profile shows a small bump around $r \sim 130$ au, corresponding to the radius of the dust ring beyond the dust gap.

Using the $I_{\nu,\mathrm{peak}}$ profiles, we derive the peak brightness temperature ($T_{\mathrm{B,peak}}$) by assuming $I_{\nu,\mathrm{peak}} = \mathrm{B}_{\nu}(T_{B,\mathrm{peak}})$, where B_{ν} is the Planck function at a given frequency ν. The derived $T_{B,\mathrm{peak}}$ profiles are presented in Figure 4(d). The color-shaded regions are the uncertainties of $T_{\mathrm{B,peak}}$ due to those of $I_{\nu,\mathrm{peak}}$ in Figure 4(c). As with the $I_{^{13}\mathrm{CO,peak}}$ profile, the derived $T_{\mathrm{B,peak}}$ profile from the ^{13}CO line also shows a small bump at $\sim$130 au.

To quantify the temperature bump at $\sim$130 au, we perform the least-squares fit to the derived $T_{\mathrm{B,peak}}$ profiles using the power-law profile with a single Gaussian,

$$T_{B,\mathrm{peak}}(r) = A\left(\frac{r}{50\ \mathrm{au}}\right)^{B} + C\ \exp\left(-\frac{(r-D)^2}{2E^2}\right), \qquad (2)$$

where A, B, C, D, and E are the fitting parameters. Using the data within 20 au $\leqslant r \leqslant$ 200 au, we obtain the fitting parameters, as summarized in Table 3. The fitting parameters show that the small bump of $T_{\mathrm{B,peak},^{13}\mathrm{CO}}$ profile at $r \sim 127$ au has $\sim$4.3 K amplitude, corresponding to $\sim 1.4\sigma$ at this radius

Table 3
Fitting Parameters of the Peak Brightness Temperature Profiles of the ^{12}CO and ^{13}CO Lines

Species	A (K)	B	C (K)	D (au)	E (au)
^{12}CO	37.57 ± 1.38	−0.38 ± 0.02	8.37 ± 0.91	82.81 ± 4.65	36.05 ± 5.69
^{13}CO	28.29 ± 0.38	−0.54 ± 0.03	4.31 ± 0.69	127.62 ± 3.33	21.96 ± 4.86

Table 4
Gaussian Fitting Parameters for the Dust Gap

$T_{\rm dust}$	$r_{\rm cent}$ (au)	Δr (au)	$\Sigma_{\rm peak}$ (g cm^{-2})	Depth (%)
$T_{B,{\rm peak},^{12}{\rm CO}}$	88.94	9.74	0.028	∼21.71
$T_{B,{\rm peak},^{13}{\rm CO}}$	91.47	6.72	0.038	∼19.94

($1\sigma \approx 3$ K). The dashed lines in Figure 4(d) present the fitting results of $T_{\rm B,peak}$ profiles.

The $T_{\rm B,peak}$ profile derived from $I_{^{12}{\rm CO,peak}}$ also has a small bump at $r \sim 82$ au, the inner edge of the dust gap. It may be related to the slope change of the dust continuum intensity. The location of the photosphere of the ^{12}CO line could change inside and outside of the dust-rich disk. The disk scale height could also change there (see Section 4.4). The difference between the ^{12}CO and ^{13}CO brightness temperatures can be a hint for the temperature and density distribution of the gas disk. We will discuss it more in Section 4.4.2.

4. Discussion

4.1. The Dust Gap in the CR Cha Disk

To analyze the dust gap structure of the CR Cha disk, we derive the radial profile of dust surface density ($\Sigma_{\rm dust}$) from the observed dust continuum intensity. We derive the optical depth at 225 GHz, $\tau_{225\ {\rm GHz}}$, using the radiative transfer equation, $I_{\rm cont} = {\rm B}_{225\ {\rm GHz}}({\rm T}_{\rm dust})(1 - \exp(-\tau_{225\ {\rm GHz}})$, where we simply assume that the dust temperature is equal to the gas temperature derived from the moment 8 maps of the ^{12}CO or ^{13}CO line in Figure 4(d), that is, $T_{\rm dust} = T_{\rm gas} = T_{\rm B,peak}$. We note that since both CO lines are optically thick, we can use the derived $T_{\rm B,peak}$ profiles as the gas temperature ($T_{\rm gas}$) profiles of the ^{12}CO and ^{13}CO line emitting regions. And then we derive the dust surface density $\Sigma_{\rm dust}$ using the equation $\tau_{225\ {\rm GHz}} = \kappa_{225\ {\rm GHz}}\Sigma_{\rm dust}$, where $\kappa_{225\ {\rm GHz}} = 2.3$ cm^2 g^{-1} (e.g., Beckwith et al. 1990) is the dust opacity at 225 GHz.

The solid lines in Figure 5 present the derived $\tau_{225\ {\rm GHz}}$ and $\Sigma_{\rm dust}$ profiles when the $T_{\rm dust}$ equals $T_{\rm B,peak,^{12}CO}$ (red) and $T_{\rm B,peak,^{13}CO}$ (blue). The color-shaded regions indicate the uncertainties of $\tau_{225\ {\rm GHz}}$ and $\Sigma_{\rm dust}$ propagated from those of the peak brightness temperature in Figure 4(d). We note that although we simply assume $T_{\rm dust} = T_{\rm gas}$, the dust temperature near the disk midplane could be lower than the gas temperature of the ^{13}CO or ^{12}CO line emitting regions (see Section 4.4.2). Thus, the derived dust surface density could be lower than the actual dust surface density.

We adopt a single Gaussian function to estimate the dust gap structure at $r \sim 90$ au. As the baseline of dust surface density profile, we adopt the power-law function with an exponential tail,

$$\Sigma_{d,{\rm baseline}} = A\left(\frac{r}{50\ {\rm au}}\right)^{-0.5}\exp\left[-\left(\frac{r}{100\ {\rm au}}\right)^4\right], \quad (3)$$

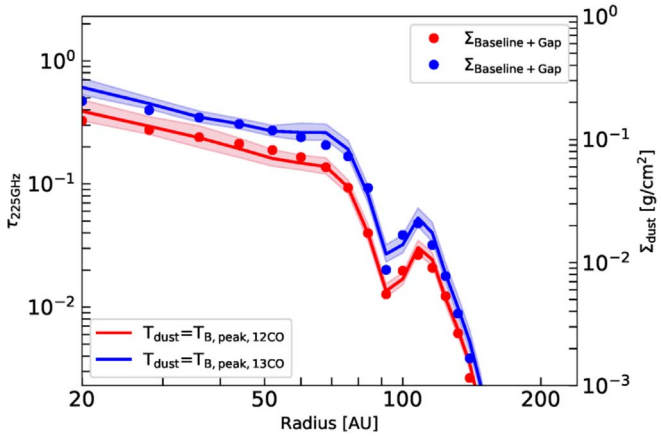

Figure 5. Radial profiles of optical depth at 225 GHz ($\tau_{225\ {\rm GHz}}$) and the dust surface density ($\Sigma_{\rm dust}$), where $\tau_{225\ {\rm GHz}} = \kappa_{225\ {\rm GHz}}\Sigma_{\rm dust}$ with the constant $\kappa_{225\ {\rm GHz}} = 2.3$ cm^2 g^{-1}. The solid lines present the derived $\tau_{225\ {\rm GHz}}$ and $\Sigma_{\rm dust}$ profiles when we adopt the peak brightness temperature of ^{12}CO (red) and ^{13}CO (blue) as dust temperature. The color-shaded regions indicate the uncertainties propagated from those of the peak brightness temperature in Figure 4(d). The Gaussian fitting results of the baseline plus dust gap expressed in Equations (3) and (4) are shown as dotted lines with the same color indications. The fitting parameters summarized in Table 4 show that the dust gap is centered at $r \sim 90$ au with a width of ∼8 au on average. The depth of the gap at the center is ∼20% on average.

where $A = 0.09$ g cm^{-2} for $T_{\rm dust} = T_{\rm B,peak,^{12}CO}$ and $A = 0.13$ g cm^{-2} for $T_{\rm dust} = T_{\rm B,peak,^{13}CO}$. We note that the terms of Equation (3) are derived by the least-squares fitting to reproduce the shape of the profiles. And then, we choose concrete numbers within the uncertainties of the fitting parameters. After subtracting the baseline from the derived $\Sigma_{\rm dust}$ profiles, the gap structure is fitted using a single Gaussian function,

$$\Sigma_{d,{\rm gap}} = \Sigma_{\rm peak}\exp\left[\frac{(r - r_{\rm cent})^2}{2(\Delta r)^2}\right]. \quad (4)$$

Table 4 summarizes the Gaussian fitting parameters for the gap structure. The uncertainties of the fitting parameters are more than 500% for all parameters owing to the small number of data points in the gap: only two to three data points are included in the gap width of ∼8 au owing to 8 au width of annuli for the azimuthal average under the beam size of ∼0.″087 (∼16 au at $d \sim 187.5$ pc).

The dotted lines in Figure 5 present the fitting results of the baseline plus dust gap. For both cases, the fitting results show that the dust gap is centered at $r \sim 90$ au and has a width of ∼8 au on average. The depth of the gap is measured as $(\Sigma_{d,{\rm baseline}}(r_{\rm cent}) - \Sigma_{\rm peak})/\Sigma_{d,{\rm baseline}}(r_{\rm cent})$, the ratio between the bottom of the gap and the baseline value at the gap center $r_{\rm cent}$. The derived gap depth is ∼20% on average. We note that the derived gap depth should be regarded as the upper limit owing to the larger synthesized beam size (∼16 au) than the estimated

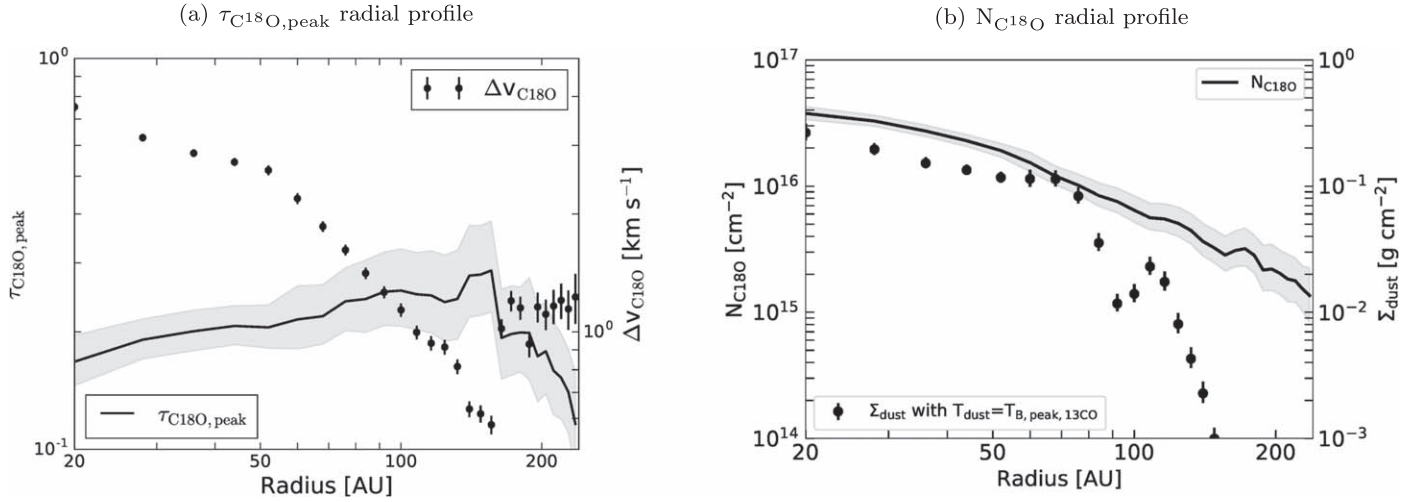

Figure 6. (a) Radial profile of $\tau_{C^{18}O,peak}$ (solid line) with the uncertainty (gray-shaded regions). The dotted line with error bars indicates the fitted width of the averaged $C^{18}O$ line spectra at each annulus. The optical depth in the inner disk decreases owing to the line broadening caused by the high rotation velocity in the very inner disk. This line broadening leads to a small Gaussian peak. (b) Radial profiles of the $C^{18}O$ column density $N_{C^{18}O}$ (solid line) with the uncertainty (gray-shaded region). The dotted line with error bars indicates the dust surface density profile derived using $T_{dust} = T_{B,peak,^{13}CO}$ in Section 4.1. The gas disk is extended much farther than the dust disk.

gap width of ∼8 au. The observed intensity profile can be reproduced by a deeper and narrower gap than those derived from our observation. As an example, the observation of the HD 163296 disk with high angular resolution (∼0.″05, Isella et al. 2018) shows that the gap is deeper than that observed with low angular resolution (∼0.″2; Isella et al. 2016).

4.2. $C^{18}O$ Gas Column Density

In this section, we analyze the CO gas radial distribution in the CR Cha disk. We adopt the following equation in Yamamoto (2017) to derive the $C^{18}O$ column density ($N_{C^{18}O}$):

$$\int \tau_\nu dv \approx \sqrt{2\pi}\ \tau_{\nu,\mathrm{peak}} \Delta v = \frac{8\pi^3 S\mu_0^2}{3hU(T_{\mathrm{gas}})}\left[\exp\left(\frac{h\nu}{k_B T_{\mathrm{gas}}}\right) - 1\right] \times \exp\left(-\frac{E_u}{k_B T_{\mathrm{gas}}}\right) N_{\mathrm{molecule}}, \quad (5)$$

where $\tau_{\nu,\mathrm{peak}}$ is the peak optical depth of the molecular line at the line center, Δv is the width of the molecular line, S is the molecular line strength, μ_0 is the permanent dipole moment of the molecule, h is the Planck constant, $U(T_{\mathrm{gas}})$ is the rotational partition function of the molecular species at a given gas temperature T_{gas}, ν is the rest frequency of the molecular transition line, k_B is the Boltzmann constant, E_u is the upper-state energy level, and N_{molecule} is the column density of the molecule. We simply assume that the line optical depth has a Gaussian profile with the peak value of $\tau_{\nu,\mathrm{peak}}$ and the width of Δv for $\int \tau_\nu dv \approx \sqrt{2\pi}\,\tau_{\nu,\mathrm{peak}}\Delta v$.

For the $C^{18}O$ $J = 2$–1 transition line, we adopt $\nu = 219.5603$ GHz, $S\mu_0^2 = 0.02440\ \mathrm{D}^2 \approx 2.440 \times 10^{-51}\ \mathrm{J} \times \mathrm{m}^3$, and $E_u/k_B = 15.80580$ K from the Leiden Atomic and Molecular Database (Schöier et al. 2005) and the Cologne Database for Molecular Spectroscopy (Müller et al. 2001). The rotational partition function $U(T_{\mathrm{gas}})$ of the $C^{18}O$ molecule is approximated as $U(T_{\mathrm{gas}}) \approx 0.38(T_{\mathrm{gas}} + 0.88)$ (Mangum & Shirley 2017).

As a first step, we derive the peak optical depth at the $C^{18}O$ line center ($\tau_{C^{18}O,peak}$) using the radiative transfer equation, $I_{C^{18}O,peak} = B_{C^{18}O}(T_{\mathrm{gas}})[1 - \exp(-\tau_{C^{18}O,peak})]$, with $T_{\mathrm{gas}} = T_{B,peak,^{13}CO}$, the blue line in Figure 4(d). The $I_{C^{18}O,peak}$ is derived from the Gaussian fitting of the azimuthally averaged $C^{18}O$ line spectra of every 8 au width annulus within $r \lesssim 240$ au. When we azimuthally average the $C^{18}O$ line spectra, we shift the velocity offset of the line at each point in the annulus (mainly due to Doppler shift by the Keplerian rotation) by using the moment 1 map of the $C^{18}O$ line.

From the azimuthally averaged line spectra, we obtain the peak $C^{18}O$ line intensity ($I_{C^{18}O,peak}$) and the width ($\Delta v_{C^{18}O}$) by Gaussian fitting. The peak optical depth of the $C^{18}O$ line ($\tau_{C^{18}O,peak}$) is presented in Figure 6(a) as a solid line. The gray-shaded region shows the uncertainty of the $\tau_{C^{18}O,peak}$. The dotted line with error bars in the same figure shows the fitted line width $\Delta v_{C^{18}O}$. The decrease of $\tau_{C^{18}O}$ in the inner disk is caused by the line broadening. Since the Keplerian rotation velocity is higher and the gradient of velocity along the line of sight is steeper, the beam-averaged line width becomes broader in the inner disk. Due to this line broadening, the $\tau_{C^{18}O,peak}$ profile is nearly flat up to $r \sim 160$ au, but the line width rapidly decreases. In the outer disk of $r \gtrsim 160$ au, the Gaussian fitting is affected by the noise next to the line signal, making broader line width and smaller peak intensity. It makes the drop of $\tau_{C^{18}O,peak}$ at $r > 160$ au.

Finally, we derive the $C^{18}O$ column density ($N_{C^{18}O}$) by inserting the derived $\tau_{C^{18}O,peak}$, $\Delta v_{C^{18}O}$, and $T_{\mathrm{gas}} = T_{B,peak,^{13}CO}$ into Equation (5). Figure 6(b) shows the derived $N_{C^{18}O}$ profile as a solid line and their uncertainty as a gray-shaded region. Compared with the derived dust surface density profile, the dotted line with error bars, the $C^{18}O$ gas disk is much more extended than the dust disk. There is no gas gap around the dust gap at $r \sim 90$ au owing to the large synthesized beam size of the line observation.

4.3. The Dust-to-CO-gas Mass Ratio

The dust-to-gas mass ratio is one of the important parameters for understanding the physical and chemical conditions of the protoplanetary disks. Based on the radial profiles of dust

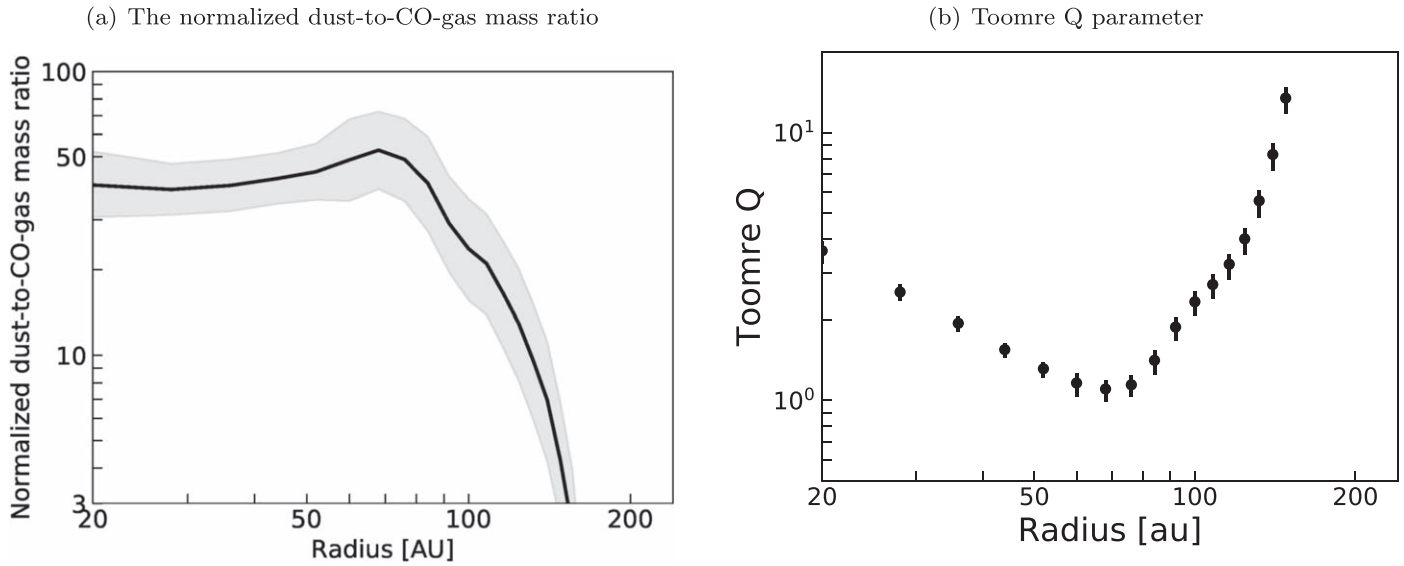

Figure 7. (a) Radial profile of dust-to-CO-gas mass ratio (ϵ/X) normalized by the typical ratio in the ISM (ϵ_0/X_0). The $\Sigma_{\rm dust}$ profile is convolved with the same beam size of the $C^{18}O$ line image for deriving the dust-to-CO-gas mass ratio. The gray-shaded region indicates the uncertainty of the ratio. The disk region in $r \lesssim 80$ au has ~50 times higher dust-to-CO-gas mass ratio than the typical ISM. Outside of the dust ring at 120 au, the ratio rapidly decreases toward unity. (b) Toomre's Q parameter of the disk derived from the $\Sigma_{\rm dust}$ in Figure 6(b) and the assumption of $\Sigma_{\rm disk} \approx \Sigma_{\rm gas} = 100\Sigma_{\rm dust}$. The region $r \lesssim 80$ au has $Q \approx 1$–3, which is a marginally gravitationally unstable disk.

surface density and $C^{18}O$ column density in Sections 4.1 and 4.2, we derive the dust-to-CO-gas mass ratio of the CR Cha disk.

When we adopt the factor $X \equiv N_{\rm CO}/N_{\rm H_2}$, the ratio of the number density between CO and H_2 molecules, and $\epsilon \equiv \Sigma_{\rm dust}/\Sigma_{\rm H_2}$, the dust-to-gas mass ratio, we derive the dust-to-CO-gas mass ratio

$$\frac{\epsilon}{X} = \frac{\Sigma_{\rm dust}}{\Sigma_{\rm H_2}}\frac{N_{\rm H_2}}{N_{\rm CO}} = \frac{\Sigma_{\rm dust}}{2m_{\rm H}N_{\rm CO}} = 14\,\frac{\Sigma_{\rm dust}}{\Sigma_{\rm CO}}, \quad (6)$$

where $\Sigma_{\rm H_2} = 2m_{\rm H}N_{\rm H_2}$, $\Sigma_{\rm CO} = 28m_{\rm H}N_{\rm CO}$, and $m_{\rm H} = 1.67 \times 10^{-24}$ g is the mass of hydrogen atoms. If we adopt the typical abundance ratio of $^{12}CO/C^{18}O = 444$ (e.g., Qi et al. 2011), the CO number density is derived by the conversion of $N_{\rm CO} = 444\,N_{\rm C^{18}O}$. We adopt the typical values in the ISM of $X_0 = 10^{-4}$ and $\epsilon_0 = 10^{-2}$ for the comparison to the typical dust-to-CO-gas mass ratio in the ISM.

Figure 7(a) presents the radial profile of the normalized dust-to-CO-gas mass ratio $(\epsilon/X)/(\epsilon_0/X_0)$, indicating how the dust-to-CO-gas mass ratio of the CR Cha disk deviates from the typical ISM value. The gray-shaded region indicates the uncertainty of the dust-to-CO-gas mass ratio based on the uncertainties of the derived $\Sigma_{\rm dust}$ and $N_{\rm C^{18}O}$. We note that the $\Sigma_{\rm dust}$ profile is convolved with the same beam size of the $C^{18}O$ line image for deriving the dust-to-CO-gas mass ratio. In the disk radius of $r \lesssim 80$ au, the dust-to-CO-gas mass ratio is ~50 times higher than the typical ISM value.

The dust concentration by the radial drift of dust grains is one of the possible mechanisms to explain this high dust-to-CO-gas mass ratio in the inner disk. Here, we simply assume that the initial dust disk is extended to $r = 240$ au with a uniform dust surface density and the dust mass is conserved during the radial contraction. If only dust grains drift inward down to $r \sim 90$ au from $r = 240$ au, ~9 times dust concentration is acceptable. However, it is still not enough to reach ~50 times higher dust-to-CO-gas mass ratio, so that they may need other causes to increase the dust-to-CO-gas mass ratio. The CO gas depletion ($X = N_{\rm CO}/N_{\rm H_2} < 10^{-4}$) and/or gas dispersal ($\epsilon = \Sigma_{\rm dust}/\Sigma_{\rm gas} > 0.01$) may have to be considered as another possibility to explain this high dust-to-CO-gas mass ratio.

We note that there are some uncertainties in the derived dust-to-CO-gas mass ratio. As mentioned in Section 4.2, the dust surface density could be underestimated because the temperature at the disk midplane, where optically thin dust continuum will be mainly emitted, is possibly lower than the temperature of the ^{13}CO line emitting region in the disk surface. In that case, the dust-to-CO-gas mass ratio could be underestimated. Also, the dust opacity has large uncertainty, which also leads to uncertainty in derived dust surface density. Meanwhile, if the $C^{18}O$ line is optically thick, the derived $C^{18}O$ column density will be underestimated. Thus, the derived dust-to-CO-gas mass ratio could be overestimated.

Although we can reproduce the observed high dust-to-CO-gas ratio with dust concentration, gas dispersal, or CO depletion, this high dust-to-CO-gas mass ratio can trigger the gravitational or streaming instabilities. The disk stability by self-gravity is presented by the Toomre Q parameter (Toomre 1964),

$$Q \equiv \frac{c_s\Omega_{\rm K}}{\pi G\Sigma_{\rm disk}}, \quad (7)$$

where c_s is sound speed, $\Omega_{\rm K}$ is orbital frequency, G is the gravitational constant, and $\Sigma_{\rm disk}$ is disk surface density. The assumptions of $T = T_{\rm B,peak,^{13}CO}$ and $M_\star = 1.657\,M_\odot$ are used for deriving $c_s = \sqrt{kT/\mu m_{\rm H}}$ and $\Omega_{\rm K} = \sqrt{GM_\star/r^3}$. If the observed high dust-to-CO-gas mass ratio is explained only by the CO gas depletion and there is no gas dispersal or dust concentration ($\Sigma_{\rm disk} \approx \Sigma_{\rm gas} = 100\Sigma_{\rm dust}$), the derived Toomre Q parameter is $Q \sim 1$–3 inside of $r \sim 100$ au, shown in Figure 7(b), indicating that the disk is marginally unstable by self-gravity. Meanwhile, if there is gas dispersal and/or dust concentration, Figure 9 in Yang et al. (2017) shows that $\Sigma_{\rm dust}/\Sigma_{\rm gas} \gtrsim 0.2$ triggers the streaming instability regardless of

the grain sizes. It indicates that $(\epsilon/X)/(\epsilon_0/X_0) \gtrsim 20$ can trigger the streaming instability if we assume no CO gas depletion (that is, $X = N_{\rm CO}/N_{\rm H_2} = 10^{-4}$). If these instabilities are triggered, the dust disk is rapidly dissipated by creating planetesimals or disk substructures like spiral arms and cannot stand for a long time (e.g., Dong et al. 2015a; Li et al. 2019). Since it is not consistent with the observation, some assumptions used in the derivations of dust and gas surface density from our observations may not be realistic.

4.4. The Formation of Dust Gap-ring Structure

In this section, we discuss the possible formation mechanisms of the dust gap-ring structure in the outer region of the dust disk. Here we introduce two possible mechanisms: gap opening by a planet, and dust concentration on the gas pressure bump at the outer edge of the dust disk.

4.4.1. Gap Opening by a Planet

The surface density distribution of the gap formed by a planet is well studied by numerical simulations in previous studies. Here, we compare the surface density distribution around the gap obtained from the observations with the numerical models to constrain the planet mass that can reproduce the observed gap structure.

We adopt the model of Rosotti et al. (2016) to estimate the minimum planet mass for reproducing the dust gap structure in the CR Cha disk. They suggest that the minimum planet mass that can perturb the dust surface density is

$$M_{\rm p,min} \sim 15\, M_\oplus \left(\frac{H/R}{0.05}\right)^3 \left(\frac{M_*}{1\, M_\odot}\right), \quad (8)$$

where H is the disk vertical scale height, R is the radial location of the planet, and M_* is the central star mass. To evaluate H/R, we use $T = 22$ K at the gap center of $r_{\rm cent} = R = 91.47$ au, which are obtained from ^{13}CO line emission and from the dust surface density distribution. Assigning $M_* = 1.657\, M_\odot$ (Villebrun et al. 2019) and $H/R = 0.0683$ into Equation (8), we obtain $M_{\rm p,min} \sim 0.2\, M_{\rm J}$. This is the lower limit of the planet mass for creating a dust gap in the CR Cha disk.

Next, we evaluate the planet mass in the gap through the fitting of the observed gap structure using Equations (6)–(10) in Kanagawa et al. (2017). In Kanagawa et al. (2017), the surface density profile is controlled by two parameters, K and K':

$$K = \left(\frac{M_{\rm p}}{M_*}\right)^2 \left(\frac{h_{\rm p}}{R_{\rm p}}\right)^{-5} \alpha^{-1}, \quad (9)$$

$$K' = K \left(\frac{h_{\rm p}}{R_{\rm p}}\right)^2, \quad (10)$$

where $M_{\rm p}$ is the planet mass, M_* is the central star mass, $h_{\rm p}$ is the disk scale height at the planet orbital radius $R_{\rm p}$, and α is the dimensionless parameter for the strength of the turbulence (Shakura & Sunyaev 1973). To evaluate these parameters, we use the same parameters used above: $T = 22\ K$, $r_{\rm cent} = 91.47$ au. The gap center is also used as the planet orbital radius $R_{\rm p}$. Using these values, we find that the parameters K and K' depend on a single parameter $\alpha^{-1}(M_{\rm p}/M_*)^2$.

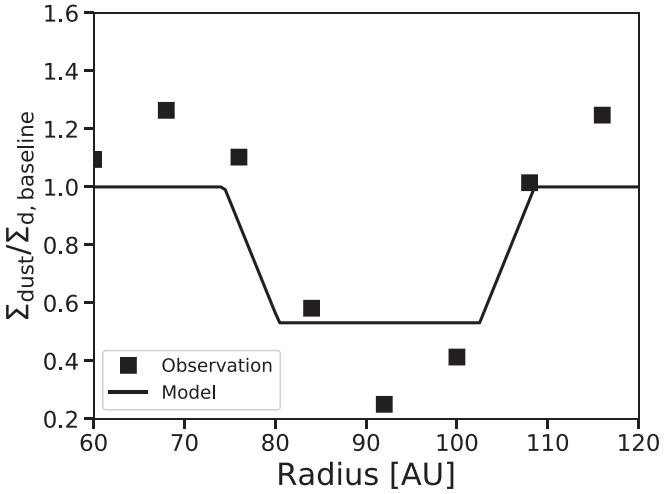

Figure 8. Comparison between the surface density profiles derived from our observation (filled squares) and those predicted by the gap opening model (solid line). The vertical axis is the surface density normalized by the baseline function expressed as Equation (3).

Figure 8 shows the comparison between the surface density distributions derived from the observation (filled square) and those predicted by the model of gap opening by a planet (solid line). We note that we normalize the observed dust surface density by the baseline function Equation (3) for the fitting to the model. The best-fit value is $\alpha^{-1}(M_{\rm p}/M_*)^2 = 3.3 \times 10^{-5}$. Thus, the planet mass that can open the observed gap structure is

$$M_{\rm p} = 0.99 M_{\rm J} \left(\frac{\alpha}{0.01}\right)^{0.5}, \quad (11)$$

where $M_{\rm J}$ is the Jupiter mass. Note that the planet mass estimated here has a large uncertainty caused by the resolution of the observations and the dust evacuation from the gap as mentioned above.

We note that there are two uncertainties for this planet mass estimation. First, the observed gap structure is not well resolved by the beam as mentioned in Section 4.1. Thus, the gap in the dust surface density would be deeper than that obtained from the observations. Second, the depth of the dust gap may be much deeper than that of the gas gap. We assume that the dust gap structure obtained from our observation can trace the gas gap structure. This assumption will be justified when the dust grain size is small enough that the dust grains are tightly coupled with the gas. In contrast, dust particles will be evacuated from the gas gap if the dust particles grow to about millimeter size (de Juan Ovelar et al. 2013; Dong et al. 2015b). In this case, we obtain the depth of the gas gap larger than the real, which concludes a more massive planet mass to reproduce the observed gap depth.

We also estimate the upper limit of the planet mass from the cases in which the gas gap is too shallow or too wide to be nondetection within the uncertainties of our observation. The ratio of the derived lower and upper limit of $N_{\rm C^{18}O}$ at 100 au is ~0.6. If we assume that the upper limit is the baseline value and the lower limit is the bottom of the gas gap,

$$\frac{\Sigma_{\rm lower}}{\Sigma_{\rm upper}} = \frac{1}{1 + 0.04{\rm K}} > 0.6. \quad (12)$$

When we assign $R_{\rm p} = 91.47$ au, $T = 22$ K, and $M_* = 1.657\, M_\odot$ into Equation (12), the estimated upper limit of the

planet mass is

$$M_{\rm p} < 0.87 M_{\rm J}\left(\frac{\alpha}{0.01}\right)^{1/2}. \quad (13)$$

Similarly, if the gas gap has a comparable width to the synthesized beam size of our observation, we also cannot detect the gas gap in the $N_{\rm C^{18}O}$ profiles. The relation between the gap width and the planet mass is expressed as

$$\Delta R = 0.33 {\rm K}'^{1/4} R_{\rm p}. \quad (14)$$

Considering the beam size of $\sim 0\farcs2$ corresponding to $\sim$37.6 au at 187.5 pc in physical scale, the upper limit of the planet mass is derived as

$$M_{\rm p} < 1.2 M_{\rm J}\left(\frac{\alpha}{0.01}\right)^{1/2}. \quad (15)$$

Those values conclude that about Jupiter-mass planets are required to reproduce the observed dust gap structures regardless of the existence of the gas gap at the dust gap location. The scattered-light imaging is a good next step to investigate the planet mass estimation and gap structures by their higher spatial resolutions and direct tracing of small dust grains that are generally well coupled with the gas (e.g., Dong & Fung 2017).

The temperature bump around 130 au could be related to the heating of the outer wall of the gap. According to the previous studies, the gap opening by a planet changes the temperature distribution around the gap structure (e.g., Jang-Condell & Turner 2012; Turner et al. 2012). Due to the smaller surface density inside the gap structure, this region can be heated by the stellar radiation, which can penetrate to a deeper layer of the disk.

4.4.2. Dust Concentration on the Gas Pressure Bump

Here we discuss another possible formation mechanism of the dust gap-ring structure in the outer region of the dust disk. We assume the situation that the dust disk becomes more compact than the gas disk through the radial drift of the dust grains in the disk. At the outer edge of the dust disk, the transition of optical depth occurs owing to the steep decrease of dust surface density. Then, the temperature at the midplane increases by the direct irradiation heating from the hot surface layer of the disk. This temperature variation leads to the pressure bump formation just beyond the edge of the dust disk. If there is a small amount of dust grains in the outside of the dust disk, they drift inward and concentrate on the pressure bump so that the ring structure is formed. This mechanism is consistent with the observed features: a dust ring beyond the dust gap, a more compact dust disk than the gas disk, and the temperature bump in ^{13}CO line emission beyond the dust gap.

We perform the radiative transfer calculation to derive the temperature distributions in the disk r-z plane when the dust disk is more compact than the gas disk by using a published code HO-CHUNK (Whitney et al. 2003a, 2003b, 2004, 2013). We adopt the stellar mass of 1.657 $M_\odot$, the effective temperature of 4800 K, and the stellar radius of 3.113 $R_\odot$ (Villebrun et al. 2019). We also use the dust surface density derived from the observed $I_{\rm cont}$ at $T_{\rm dust} = T_{\rm B,peak,^{13}CO}$. For the radiative transfer calculations, we use the fitted dust surface density profile within the radius of 20 au $< r <$ 100 au to consider the compact dust disk. Although the dust temperature will change step by step during the radial drift of the grains in reality, here we assume a fixed dust surface density profile for simplicity. We obtain the fitted dust surface density profile of

$$\Sigma_{d,{\rm RT}} = A\left(\frac{r}{10\ {\rm au}}\right)^{B} \exp\left[-\left(\frac{r}{C\ {\rm au}}\right)^{10}\right], \quad (16)$$

where $A = 0.27 \pm 0.02$ g cm^{-2}, $B = -0.45 \pm 0.06$, and $C = 86.0 \pm 1.66$ au. It is presented as the black dashed line in Figure 9(a). The dust distribution is effectively cut off at 100 au.

In our calculation, we introduce two dust components: small dust grains and large dust grains. The minimum and maximum sizes are 0.0025 and 0.2 μm for small dust grains and 0.01 μm and 1 mm for large dust grains, respectively. The size distribution of both dust components is $n(a) \propto a^{-3.5}$, where $n(a)$ is the number density per unit radius and a is the radius of dust grains. The opacity models for both small and large dust grains are described in Hashimoto et al. (2015) (see also Kim et al. 1994; Wood et al. 2002; Dong et al. 2012). We adopt Equation (16) as the surface density distribution of large dust grains and assume that the surface density of the small dust grains is 10 times smaller than that of the large dust grains ($\Sigma_{\rm small} = 0.1\Sigma_{\rm large}$; e.g., D'Alessio et al. 2006). We note that the small-to-large dust mass ratio for the size distribution of $n(a) \propto a^{-3.5}$ is 1%. However, many practical calculations (e.g., Andrews et al. 2011; Dong et al. 2015b) use the size distribution and change the small-to-large dust mass ratio independently because the results are not very different even if the mass ratio is assumed as 10%. To obtain the density distributions of small and large dust grains, we set the scale height of them,

$$H_{\rm l} = 2\ {\rm au}\left(\frac{\rm r}{100\ {\rm au}}\right)^{1.25}, \quad (17)$$

$$H_{s} = 6.5\ {\rm au}\left(\frac{\rm r}{100\ {\rm au}}\right)^{1.25}, \quad (18)$$

where $H_{\rm l}$ and H_s are the scale heights of large and small dust grains, respectively. We assume that the scale height of small dust grains is similar to the gas scale height. The scale height of the large dust grains is assumed to be about three times smaller than that of the small dust grains.[15] Using these scale heights, we evaluate the density of small and large dust grains, whose density distributions in the z-direction are proportional to $\exp(-z^2/(2H_{\rm l,s}^2))$. We note that the dependence of model parameters on the resulting disk structures is beyond the scope of this work and remains to be explored.

Figure 9(b) shows the temperature distribution in the disk r-z plane generated by the radiative transfer calculation. We overlay the $\tau_\nu = 1$ layer (i.e., photosphere) of ^{12}CO and ^{13}CO line emissions as the solid and dashed lines. To obtain the optical depth of the CO isotopologue lines, we evaluate the surface density of ^{12}CO and ^{13}CO from the C^{18}O column density obtained from the C^{18}O line observations, shown as the red solid line in Figure 9(a). We fit the column density as follows:

$$N_{\rm C^{18}O} = A\left[1 + \left(\frac{r}{B\ {\rm au}}\right)^{C}\right]^{-1}, \quad (19)$$

where $A = (4.46 \pm 0.04) \times 10^{16}$ cm^{-2}, $B = 44.40 \pm 0.5$ au, and $C = 2.12 \pm 0.03$. It is presented as the red dashed line in

[15] If we assume that the gas surface density is 10 g cm^{-2} and turbulence strength $\alpha = 10^{-2}$ at 70 au, we obtain that the scale height of 1 mm dust, which is the maximum size of the large dust, is about three times smaller than the gas scale height. In reality, this ratio will depend on the radius, but here we assume the constant ratio for simplicity.

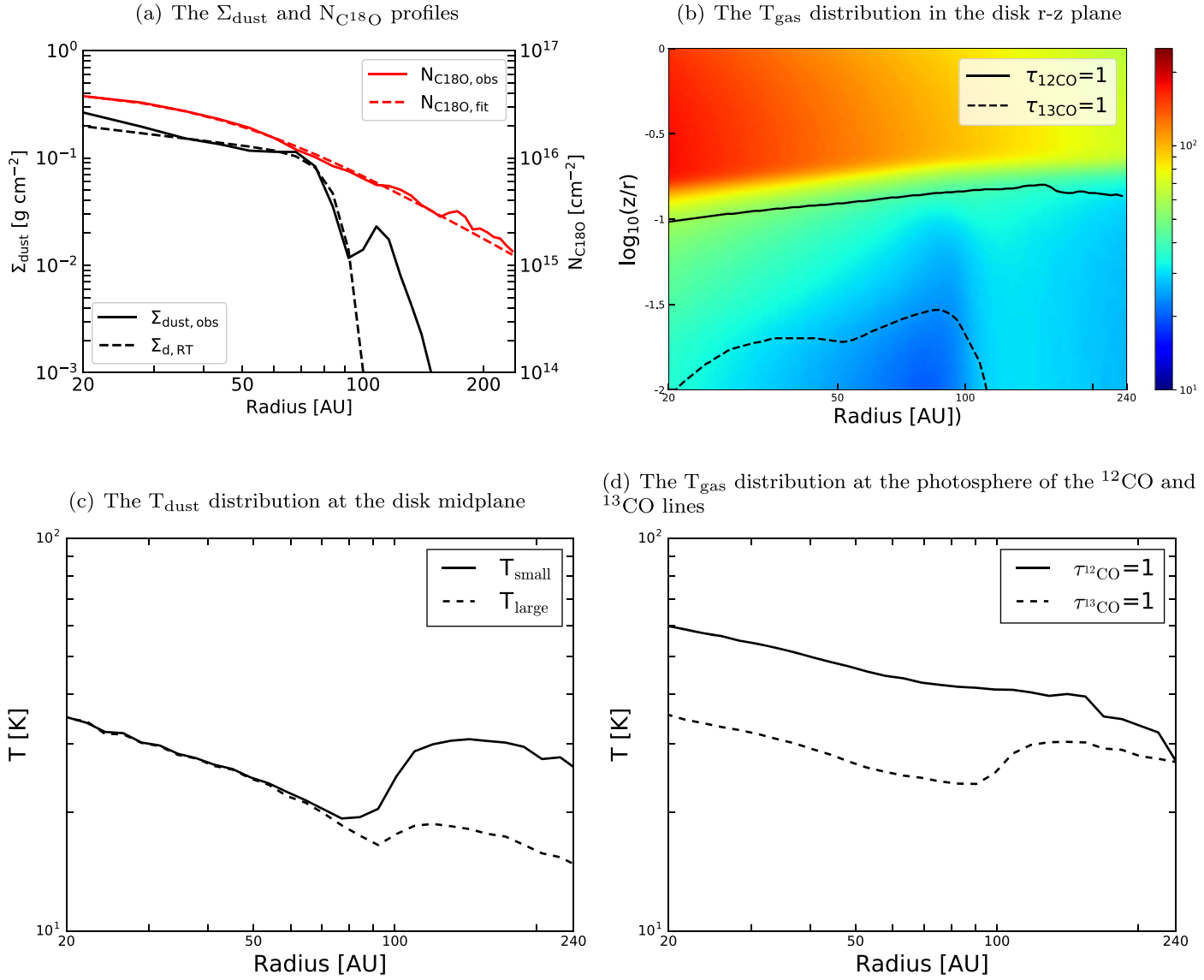

Figure 9. (a) Dust surface density profile (black) and $C^{18}O$ column density profile (red) derived from our observations (solid) and the fitting results (dashed) of Equations (16) and (19). (b) Gas temperature distribution in the disk *r*-*z* plane derived by the radiative transfer calculation. The solid and dashed lines indicate the photospheres ($\tau_\nu = 1$) of ^{12}CO and ^{13}CO emission lines, respectively. (c) Temperature distribution of the small (solid) and large (dashed) dust grains at the disk midplane. The T_{small} distribution shows a bump beyond the dust gap at 90 au. (d) Gas temperature distribution at the photosphere of ^{12}CO (solid) and ^{13}CO (dashed) emission lines shown in Figure 9(b). The gas temperature bump around 130 au is seen at the photosphere of the ^{13}CO line, but no bump at the photosphere of the ^{12}CO line.

Figure 9(a). We also assume the abundance ratios of $^{12}CO/C^{18}O = 444$ and $^{12}CO/^{13}CO = 67$ (Qi et al. 2011). Since ^{12}CO line emission is optically thick, the photosphere of the ^{12}CO line is seen at the hot upper surface of the disk. On the other hand, since the ^{13}CO line is marginally optically thick, the photosphere of the ^{13}CO line is located around or below the disk midplane.

Figure 9(c) shows the temperature distribution of dust grains at the disk midplane obtained from the radiative transfer calculations. The solid and dashed lines indicate the temperatures of small and large dust grains, respectively. The figure shows that T_{small} starts to increase at the outer edge of the dust gap at $r \sim 90$ au. In contrast, T_{large} does not increase much in the same region of the disk.

The temperature distribution can be explained as follows. The temperature at the disk midplane is determined by the balance between the heating from the hot surface layer irradiated by the stellar radiation and cooling by the dust thermal emission. In the region $r \lesssim 90$ au, the disk is optically thick against the irradiation from the hot surface layer so that the large and small dust grains have the same temperature. On the other hand, since the disk is optically thin in the region $r \gtrsim 90$ au, the small and large dust grains are directly irradiated by the hot disk surface. Since the wavelength dependence on the opacity of small dust grains is steeper than that of the large dust grains, the opacity of the small dust grains is higher for the irradiation from the hot disk surface ($\sim$30 μm) but lower for their thermal emission ($\sim$100 μm) than those of the large dust grains. Thus, the temperature of the small dust grains is higher than that of the large dust grains, resulting in the occurrence of the temperature bump in the region $r \gtrsim 90$ au. Since the gas temperature will be determined by the collisional heating with small dust grains, this temperature distribution causes the gas pressure bump around $r \sim 130$ au. If there is some amount of the dust in the region $r \gtrsim 90$ au, they can be concentrated at this gas pressure bump and form the observed ring structure. Here, we assume that there is enough dust in the

region $r > 90$ au in addition to Equation (16) to make the ring structure as a result of the radial drift of the dust and to determine the gas temperature with the small dust temperature. We need further investigation of this scenario to justify this assumption.

Figure 9(d) shows the temperature distributions at the photosphere for ^{12}CO line emission as the solid line. There is no temperature bump beyond the dust gap at 90 au since it is at the hot upper disk surface. We also show the temperature distribution at the photosphere of the ^{13}CO line emission as a dashed line, but we plot the midplane temperature if the photosphere of the ^{13}CO line is located below the midplane. Since the optical depth of ^{13}CO line emission is smaller than that of the ^{12}CO line, it traces the temperature at the layer closer to the midplane so that there is a bump in temperature distribution in the region $r \gtrsim 90$ au. This is consistent with the observed intensity bump of the ^{13}CO line around 130 au but nothing for the ^{12}CO line. On the other hand, the C^{18}O line is optically thin, and intensities in 20 and 30 K are similar in LTE condition. Thus, we cannot see the bump in the C^{18}O line either. We note that the optical depth of ^{13}CO seems lower than unity in the region of $r > 120$ au because Figure 9(c) shows only the upper half-disk in the z-direction. When integrating the full vertical disk, the optical depth of ^{13}CO becomes larger than unity up to $r \sim 160$ au but ~0.7 in the region $r > 160$ au. Considering the large uncertainty of the line ratio in Figure 3(b), it does not significantly conflict with our observations.

Meanwhile, the dust gap-ring structure in the CR Cha disk may be formed through different mechanisms. As shown in Figure 9(c), the dust temperature at the disk midplane inside the dust gap is ~20 K. Since this is comparable to the CO sublimation temperature (~15–25 K), the dust gap and ring could be created by the dust sintering effect (Okuzumi et al. 2016). Secular gravitational instability (secular GI; Ward 2000; Youdin 2011; Michikoshi et al. 2012) is another possible mechanism of dust ring structure formation (Takahashi & Inutsuka 2014). As mentioned in Section 4.3, the disk has a small Q value and/or large dust-to-CO-gas mass ratio. These features are suitable for the growth of the secular GI in the disk (Takahashi & Inutsuka 2014, 2016; Latter & Rosca 2017; Tominaga et al. 2019). Also, the existence of the dead zone is another possible cause to produce the dust gap-ring structure in the disk. If the gas gap is generated at the outer edge of the dead zone by viscous instability (e.g., Flock et al. 2015; Hasegawa & Takeuchi 2015), dust grains can be piled up there. The temperature bump at the outer edge of the gap is also generated by the heating of dust grains (e.g., Hasegawa & Pudritz 2010). To distinguish the dust gap-ring formation mechanisms, further investigations are required, for example, the size distribution of the dust particles, since the dust sintering mechanism indicates that the dust radius is small in a dust ring structure.

5. Summary

In this paper, we present the images of the dust continuum at 225 GHz and the CO isotopologue $J = 2$–1 emission lines of the CR Cha disk observed by ALMA. The observed dust continuum image shows a dust gap at $r \sim 90$ au and a faint dust ring at $r \sim 120$ au. We derive the radial profile of dust surface density to investigate the gap-ring structure by assuming the peak brightness temperature of the ^{13}CO emission line to be the dust temperature $T_{\rm dust}$. Using the Gaussian fitting, we find that the dust gap is located at the radius of 90 au and has a gap depth of ~20% at the gap center with ~8 au width on average.

We analyze ^{12}CO, ^{13}CO, and C^{18}O $J = 2$–1 emission lines to investigate the gas disk of CR Cha. The moment 8 maps, the channel maps, and the averaged spectra of the CO isotopologue lines inside the radius of 240 au show the absorption feature that might be caused by the Cha I foreground cloud at the velocity of $\sim 4.5\ {\rm km\ s^{-1}}$. The azimuthally averaged radial profiles of the integrated CO isotopologue line intensities show that the gas disk is extended up to 240 au, which is much larger than the dust disk. The ratios between the CO isotopologue line emissions are larger than 0.2 at all radii, larger than the typical abundance ratios of the CO isotopologue in the protoplanetary disks. This indicates that ^{12}CO and ^{13}CO lines are optically thick. To derive the gas temperature, we make the moment 8 maps of ^{12}CO and ^{13}CO lines without dust continuum subtraction because they are optically thick lines. The azimuthally averaged radial profile of the ^{13}CO peak intensity shows a small bump around ~130 au, which may indicate the temperature bump in the ^{13}CO line emitting region.

We investigate two possible mechanisms to reproduce the observed dust gap at 90 au, the dust ring structure at 120 au, and a bump of ^{13}CO emission line at 130 au: gap opening by a planet, and dust concentration on the gas pressure bump at the outer edge of the dust gap.

For investigating the scenario of gap opening by a planet, we compare the observed surface density distribution around the gap to the model surface density obtained by numerical simulations done by Kanagawa et al. (2017). We conclude that the planet mass of $M_{\rm p} \approx 0.99 M_{\rm J} (\alpha/0.01)^{1/2}$ can reproduce the observed dust surface density profile, where α is a dimensionless parameter of the turbulence. However, this value has large uncertainties for the following reasons: the synthesized beam size comparable to the gap width only constrains the upper limit of the gap depth, and the dust gap structure may not trace the gas gap structure. Thus, this value should be considered as a very rough estimation.

For investigating the scenario of dust concentration on the gas pressure bump at the outer edge of the dust gap, we set the radiative transfer calculation with two dust components: small and large dust grains. When the dust disk becomes more compact than the gas disk by the radial drift of the dust grains in the disk, the steep gradient of dust surface density around the outer edge of the dust disk leads to more efficient heating by the irradiation, from the hot upper disk surface to the small dust grains, than that of the large dust grains. As a result, the gas temperature bump beyond the dust disk is produced because the small dust grains are coupled with the gas. This can make the pressure bump and the dust grains may be concentrated at the pressure peak formed beyond the dust disk. Also, since the optical depth of ^{13}CO line emission is smaller than that of ^{12}CO, it traces the temperature around the midplane so that a bump of the ^{13}CO line is seen at 130 au, but not for the ^{12}CO line. We note that the dust sintering, secular GI, and the existence of the dead zone at the disk midplane also can explain the observed dust gap-ring structure and gas temperature bump beyond the dust gap qualitatively. We need further investigations to develop a quantitative interpretation in the future.

We would like to thank the referees for comments that improved this paper. This paper makes use of the following ALMA data: ADS/JAO.ALMA#2017.1.00286.S. ALMA is a partnership of ESO (representing its member states), NSF (U.S.), and NINS (Japan), together with NRC (Canada), NSC and ASIAA (Taiwan), and KASI (Republic of Korea), in cooperation with the Republic of Chile. The joint ALMA observatory is operated by ESO, AUI/NRAO, and NAOJ. Data analysis was

carried out on the Multi-wavelength Data Analysis System operated by the Astronomy Data Center (ADC), National Astronomical Observatory of Japan. This work is supported by MEXT Grants-in-Aid for Scientific Research JP17H01103, JP18H05441, and JP19K03910 and NAOJ ALMA Scientific Research grant No. 2018-10B. Y.H. is supported by the Jet Propulsion Laboratory, California Institute of Technology, under a contract with the National Aeronautics and Space Administration.

Software: HO-CHUMK (Whitney et al. 2003a, 2003b, 2004, 2013), makemask (https://github.com/kevin-flaherty/ALMA-Disk-Code/blob/master/makemask.py), CASA (v5.3; McMullin et al. 2007).

Appendix
The Channel Maps of CO Isotopologue Lines

In Figures 10–12 we present the channel maps of ^{12}CO, ^{13}CO, and C^{18}O isotopologue lines to clearly show where the absorption feature is. The black contours overlaid in each panel indicate the Keplerian rotation model with stellar mass 2 $M_{\odot}$, disk inclination 31°, and disk PA 36°.2. We used the python code[16] written by Kevin Flaherty for generating the Keplerian rotation model. At the velocity of $V \sim 4.5$ km s^{-1}, absorption features appear. The Keplerian mask shows what regions are affected by this absorption in the moment 0 and 8 maps of the CO isotopologue lines (see Figures 1 and 4).

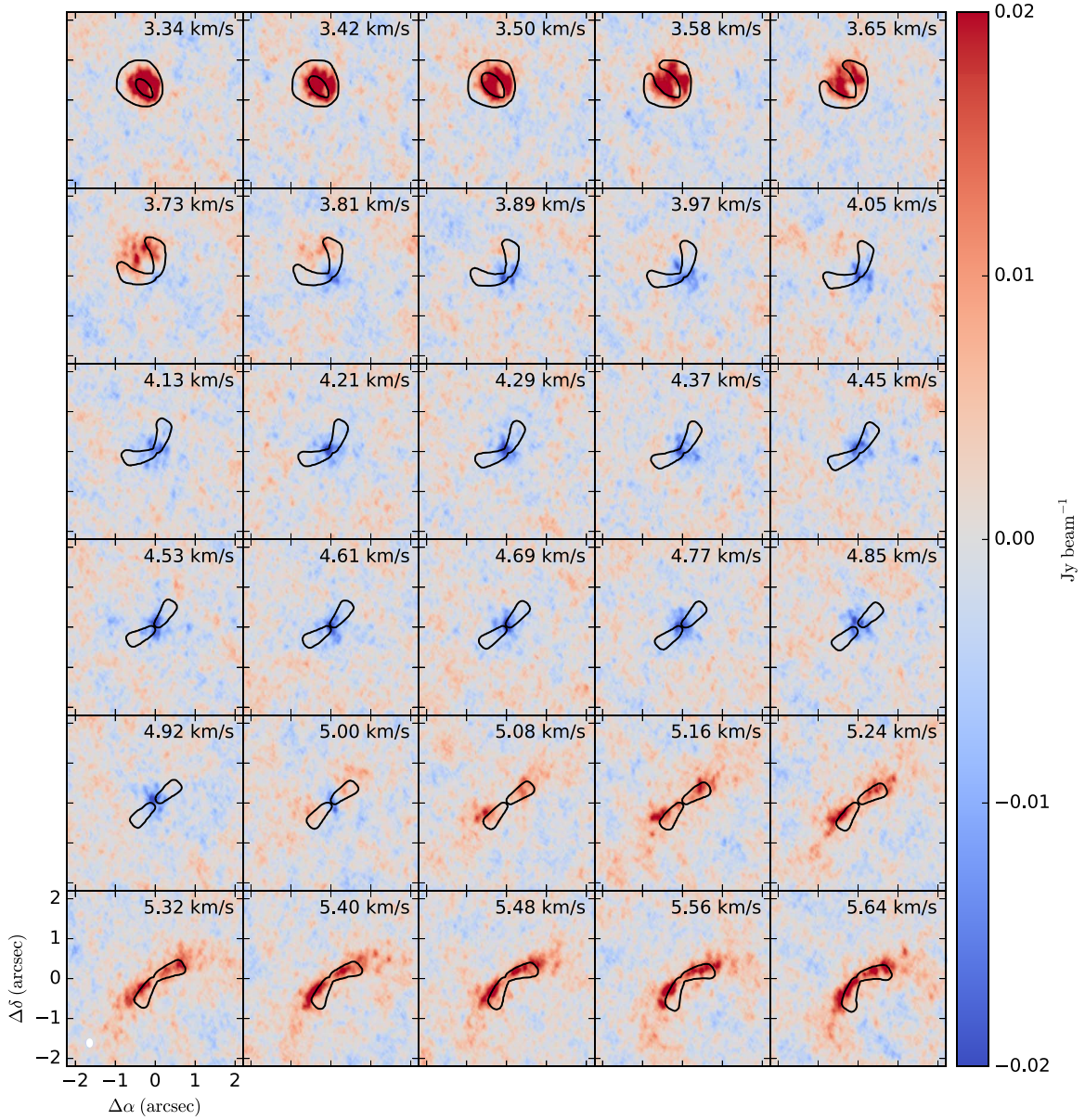

Figure 10. ^{12}CO $J = 2$–1 line channel maps from 3.3 km s^{-1} to 5.6 km s^{-1}. The channels show the absorption feature in the velocity of 3.8 km s$^{-1} < v < 5.1$ km s^{-1}. The black contours indicate the Keplerian rotation model derived by the 31° disk inclination and 36°.2 disk position angle.

[16] https://github.com/kevin-flaherty/ALMA-Disk-Code/blob/master/makemask.py

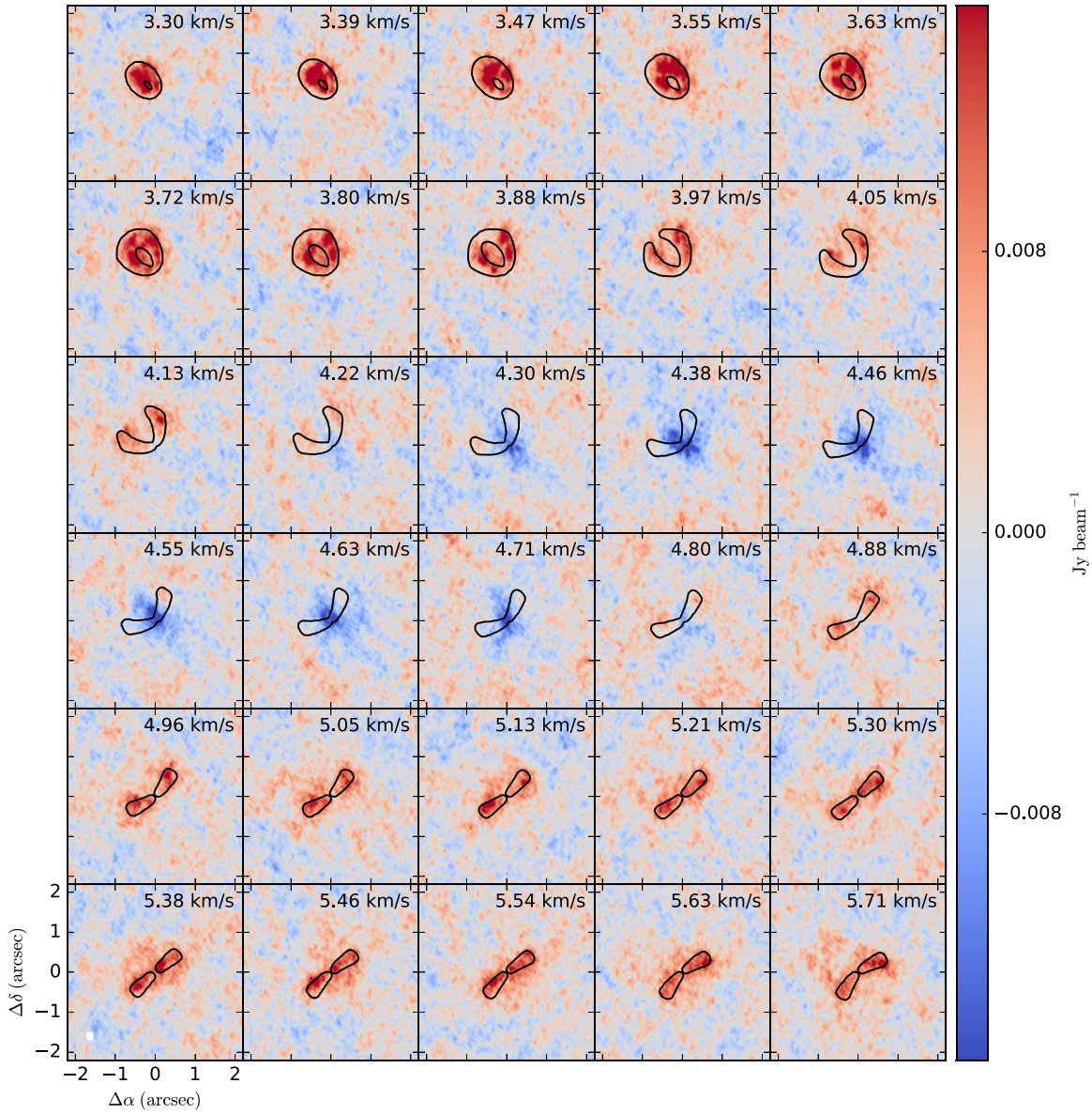

Figure 11. ^{13}CO $J = 2$–1 channel maps from 3.3 km s^{-1} to 5.7 km s^{-1}. The channels show the absorption feature in the velocity of 4.3 km s^{-1} $< v <$ 4.8 km s^{-1}. The black contours indicate the Keplerian rotation model derived by the 31° disk inclination and 36.°2 disk position angle.

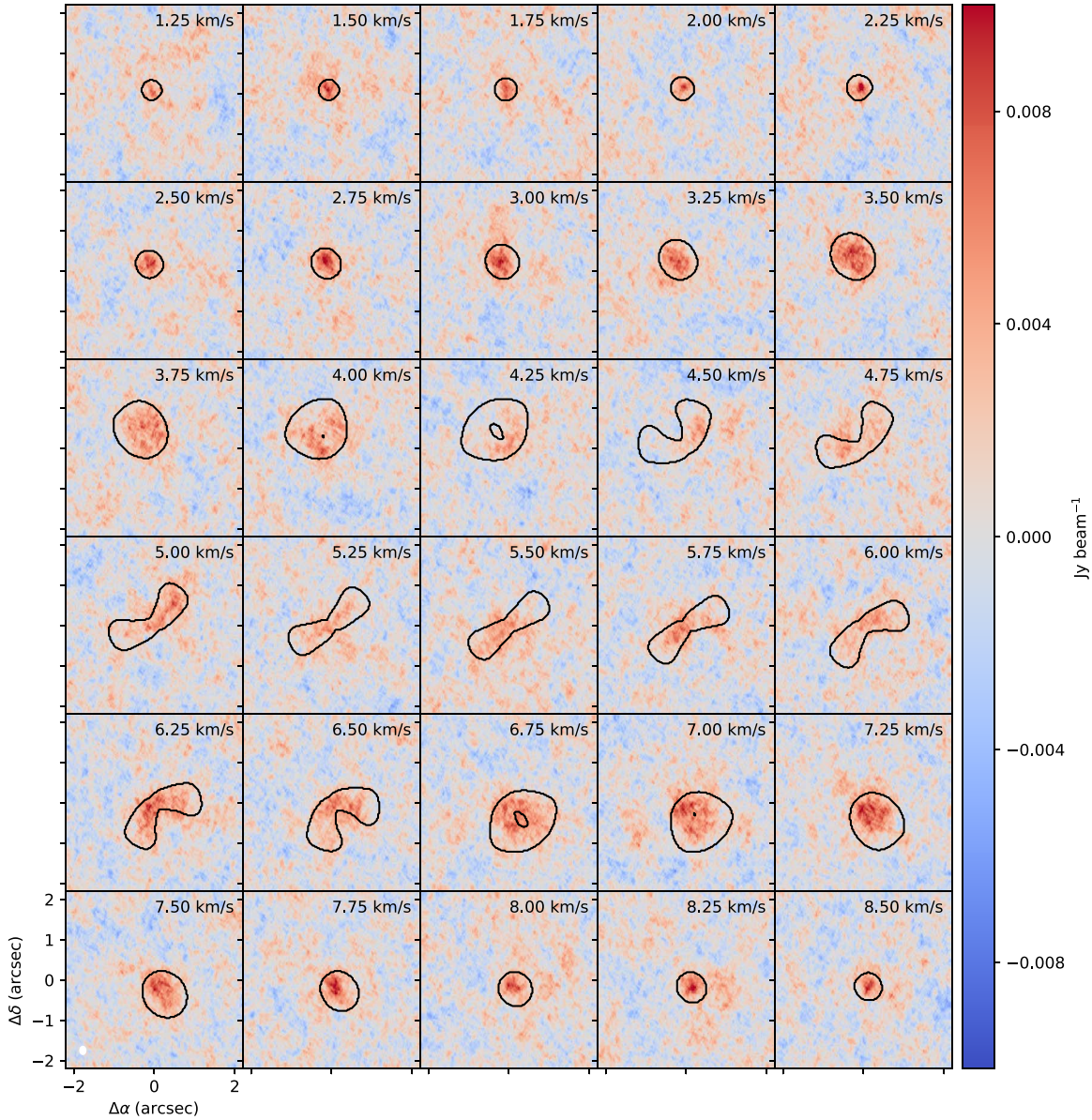

Figure 12. $C^{18}O$ $J = 2$–1 channel maps from 1.25 km s^{-1} to 8.5 km s^{-1} by smoothing the velocity resolution from 0.08 km s^{-1} to 0.25 km s^{-1} for increasing the signals. There is no clear absorption feature in the velocity of 4 km s^{-1} $< v <$ 5 km s^{-1}. The black contours indicate the Keplerian rotation model derived by the 31° disk inclination and 36.°2 disk position angle.

ORCID iDs

Seongjoong Kim https://orcid.org/0000-0003-3085-0690
Sanemichi Takahashi https://orcid.org/0000-0003-3038-364X
Hideko Nomura https://orcid.org/0000-0002-7058-7682
Takashi Tsukagoshi https://orcid.org/0000-0002-6034-2892
Ruobing Dong https://orcid.org/0000-0001-9290-7846
Jun Hashimoto https://orcid.org/0000-0002-3053-3575
Kazuhiro Kanagawa https://orcid.org/0000-0001-7235-2417
Akimasa Kataoka https://orcid.org/0000-0003-4562-4119
Mihoko Konishi https://orcid.org/0000-0003-0114-0542
Hauyu Baobab Liu https://orcid.org/0000-0003-2300-2626
Munetake Momose https://orcid.org/0000-0002-3001-0897
Michael Sitko https://orcid.org/0000-0003-1799-1755
Kengo Tomida https://orcid.org/0000-0001-8105-8113

References

Andrews, S. M., Wilner, D. J., Espaillat, C., et al. 2011, ApJ, 732, 42
Beckwith, S. V. W., & Sargent, A. I. 1991, ApJ, 381, 250
Beckwith, S. V. W., Sargent, A. I., Chini, R. S., & Guesten, R. 1990, AJ, 99, 924
Brauer, F., Dullemond, C. P., Johansen, A., et al. 2007, A&A, 469, 1169
D'Alessio, P., Calvet, N., & Hartmann, L. 2001, ApJ, 553, 321
D'Alessio, P., Calvet, N., Hartmann, L., Franco-Hernández, R., & Servín, H. 2006, ApJ, 638, 314
D'Antona, F., & Mazzitelli, I. 1994, ApJS, 90, 467
de Juan Ovelar, M., Min, M., Dominik, C., et al. 2013, A&A, 560, A111
Dong, R., & Fung, J. 2017, ApJ, 835, 146
Dong, R., Hall, C., Rice, K., & Chiang, E. 2015a, ApJL, 812, L32
Dong, R., Rafikov, R., Zhu, Z., et al. 2012, ApJ, 750, 161
Dong, R., Zhu, Z., & Whitney, B. 2015b, ApJ, 809, 93
Draine, B. T. 2006, ApJ, 636, 1114
Flock, M., Ruge, J. P., Dzyurkevich, N., et al. 2015, A&A, 574, A68
Gaia Collaboration, Brown, A. G. A., Vallenari, A., et al. 2018, A&A, 616, A1
Haikala, L. K., Harju, J., Mattila, K., & Toriseva, M. 2005, A&A, 431, 149
Hasegawa, Y., & Pudritz, R. E. 2010, MNRAS, 401, 143

Hasegawa, Y., & Takeuchi, T. 2015, ApJ, 815, 99
Hashimoto, J., Tsukagoshi, T., Brown, J. M., et al. 2015, ApJ, 799, 43
Hussain, G. A. J., Collier Cameron, A., Jardine, M. M., et al. 2009, MNRAS, 398, 189
Isella, A., Guidi, G., Testi, L., et al. 2016, PhRvL, 117, 251101
Isella, A., Huang, J., Andrews, S. M., et al. 2018, ApJL, 869, L49
Jang-Condell, H., & Turner, N. J. 2012, ApJ, 749, 153
Kanagawa, K. D., Tanaka, H., Muto, T., & Tanigawa, T. 2017, PASJ, 69, 97
Kim, S.-H., Martin, P. G., & Hendry, P. D. 1994, ApJ, 422, 164
Latter, H. N., & Rosca, R. 2017, MNRAS, 464, 1923
Li, R., Youdin, A., & Simon, J. 2019, ApJ, 885, 69
Long, F., Herczeg, G. J., Pascucci, I., et al. 2017, ApJ, 844, 99
Mangum, J. G., & Shirley, Y. L. 2017, PASP, 129, 069201
McMullin, J. P., Waters, B., Schiebel, D., Young, W., & Golap, K. 2007, in ASP Conf. Ser. 376, CASA Architecture and Applications, ed. R. A. Shaw, F. Hill, & D. J. Bell (San Francisco, CA: ASP), 127
Michikoshi, S., Kokubo, E., & Inutsuka, S.-i. 2012, ApJ, 746, 35
Miyake, K., & Nakagawa, Y. 1993, Icar, 106, 20
Müller, H. S. P., Thorwirth, S., Roth, D. A., & Winnewisser, G. 2001, A&A, 370, L49
Natta, A., Meyer, M. R., & Beckwith, S. V. W. 2000, ApJ, 534, 838
Okuzumi, S., Momose, M., Sirono, S.-i., Kobayashi, H., & Tanaka, H. 2016, ApJ, 821, 82
Pascucci, I., Testi, L., Herczeg, G. J., et al. 2016, ApJ, 831, 125
Pinilla, P., Birnstiel, T., Ricci, L., et al. 2012, A&A, 538, A114
Qi, C., D'Alessio, P., Öberg, K. I., et al. 2011, ApJ, 740, 84
Ribas, Á, Espaillat, C. C., Macías, E., et al. 2017, ApJ, 849, 63
Rosotti, G. P., Juhasz, A., Booth, R. A., & Clarke, C. J. 2016, MNRAS, 459, 2790
Schöier, F. L., van der Tak, F. F. S., van Dishoeck, E. F., & Black, J. H. 2005, A&A, 432, 369
Shakura, N. I., & Sunyaev, R. A. 1973, A&A, 500, 33
Takahashi, S. Z., & Inutsuka, S.-i. 2014, ApJ, 794, 55
Takahashi, S. Z., & Inutsuka, S.-i. 2016, AJ, 152, 184
Takeuchi, T., & Lin, D. N. C. 2005, ApJ, 623, 482
Tominaga, R. T., Takahashi, S. Z., & Inutsuka, S.-i. 2019, ApJ, 881, 53
Toomre, A. 1964, ApJ, 139, 1217
Turner, N. J., Choukroun, M., Castillo-Rogez, J., & Bryden, G. 2012, ApJ, 748, 92
Ubach, C., Maddison, S. T., Wright, C. M., et al. 2012, MNRAS, 425, 3137
Ubach, C., Maddison, S. T., Wright, C. M., et al. 2017, MNRAS, 466, 4083
Varga, J., Ábrahám, P., Chen, L., et al. 2018, A&A, 617, A83
Villebrun, F., Alecian, E., Hussain, G., et al. 2019, A&A, 622, A72
Ward, W. R. 2000, in On Planetesimal Formation: The Role of Collective Particle Behavior, ed. R. M. Canup & K. Righter (Tucson, AZ: Univ. Arizona Press), 75
Weaver, E., Isella, A., & Boehler, Y. 2018, ApJ, 853, 113
Whitney, B. A., Indebetouw, R., Bjorkman, J. E., & Wood, K. 2004, ApJ, 617, 1177
Whitney, B. A., Robitaille, T. P., Bjorkman, J. E., et al. 2013, ApJS, 207, 30
Whitney, B. A., Wood, K., Bjorkman, J. E., & Cohen, M. 2003a, ApJ, 598, 1079
Whitney, B. A., Wood, K., Bjorkman, J. E., & Wolff, M. J. 2003b, ApJ, 591, 1049
Wood, K., Wolff, M. J., Bjorkman, J. E., & Whitney, B. 2002, ApJ, 564, 887
Yamamoto, S. 2017, Introduction to Astrochemistry: Chemical Evolution from Interstellar Clouds to Star and Planet Formation (Berlin: Springer)
Yang, C. C., Johansen, A., & Carrera, D. 2017, A&A, 606, A80
Youdin, A. N. 2011, ApJ, 731, 99
Zhu, Z., Nelson, R. P., Dong, R., Espaillat, C., & Hartmann, L. 2012, ApJ, 755, 6